PHYSICAL REVIEW C

NUCLEAR PHYSICS

THIRD SERIES, VOLUME 33, NUMBER 3 MARCH 1986

# Electroexcitation of isoscalar states in $^{16}O$

T. N. Buti,[a] J. Kelly,[b] W. Bertozzi, J. M. Finn,[c] F. W. Hersman,[d] C. Hyde-Wright, M. V. Hynes,[e] M. A. Kovash,[f] S. Kowalski, R. W. Lourie, B. Murdock,[g] B. E. Norum,[h] B. Pugh, C. P. Sargent, and W. Turchinetz

*Department of Physics and Laboratory for Nuclear Science, Massachusetts Institute of Technology, Cambridge, Massachusetts 02139*

B. L. Berman[i]

*Lawrence Livermore National Laboratory, University of California, Livermore, California 94550*

(Received 29 April 1985)

We report high resolution measurements of inelastic electron scattering to all narrow normal-parity states of $^{16}O$ up to 12.05 MeV, which include states with $J_n^\pi(E_x$ MeV): $0_2^+(6.049)$, $0_3^+(12.049)$, $1_1^-(7.117)$, $2_1^+(6.917)$, $2_2^+(9.845)$, $2_3^+(11.52)$, $3_1^-(6.130)$, $4_1^+(10.356)$, and $4_2^+(11.097)$. The measurements were performed primarily at 90° and 160° and span momentum transfers between 0.6 and 2.6 $fm^{-1}$. Improved line shape fitting techniques have been developed. These are the first electron scattering measurements for the $4_2^+$ state and of second form-factor maxima for several states. The form factor for excitation of the $2_2^+$ state is strikingly different from that of the other $2^+$ states and indicates a transition density peaked in the interior. Transition charge densities were extracted from a combined data set that includes earlier electron scattering data renormalized to a recent analysis of elastic scattering from $^{16}O$. Comparisons have been made with several structure models, including the Brown-Green model, the weak-coupling model, a $2\hbar\omega$ shell model, and the tetrahedral alpha-cluster model.

## I. INTRODUCTION

The well-understood perturbative interaction between high-energy electrons and the nucleus provides an excellent probe of nuclear structure. The momentum transfer dependence of electroexcitation of nuclear transitions can be readily interpreted in terms of spatial distributions of charge, current, and magnetization. The principal motivation of the present experiment was to measure form factors for all accessible normal-parity isoscalar states of $^{16}O$ over a range of momentum transfer sufficient to extract precise radial transition densities with which to challenge theoretical structure models of this nucleus.

Perhaps the most striking feature of the spectrum of states of the $^{16}O$ nucleus is the presence of many low-lying positive parity states which cannot be described adequately in terms of the doubly-closed spherical shell model. Interestingly, the $0_2^+$ state appears at only 6.05 MeV, whereas in the spherical single-particle model it should be at about 24 MeV. Similarly, negative parity states occur at much lower excitation energy than do one-particle–one-hole (1p1h) excitations out of closed shells, and are known to contain considerable 3p3h strength. There is considerable evidence that these states are organized into collective bands based upon nonspherical components of the ground state. Some of the earliest evidence for the collective nature of these states was the rotational band systematics observed by Carter *et al.*[1] in resonances of the elastic scattering of alpha particles by $^{12}C$. Two rotational bands now appear to be firmly established. The lowest $K=0^+$ even-parity band is based upon the $0_2^+$ (6.05 MeV) state and includes the $2_1^+$ (6.92 MeV), $4_1^+$ (10.35 MeV), and $6^+$ (16.27 MeV) states. The lowest $K=0^-$ negative-parity band begins with the $1_2^-$ state at 9.63 MeV. Several other bands were proposed,[1] but more recent experimental data and theoretical models have vitiated their significance. Other evidence for the collective nature of these states includes the interband and crossband radiative decays[2,3] and the vast literature on spectroscopic data compiled in Ref. 4, some of which will be reviewed as appropriate.

The early work stimulated the coexistence model of Brown and Green,[5,6] who postulated the coexistence of spherical and deformed components in the nuclear wave functions. In their application of the coexistence idea, the deformed components were constructed from 2p2h and 4p4h excitations with axial symmetry. Several other multicomponent models posit the coexistence of a finite set of

 

intrinsic components common to all of the low-lying states.

Following the suggestion of Lowe *et al.*,[2] Goldhammer and Prosser[7] demonstrated that a two-component model, in which the ground state is dominated by a spherical component while the $0_2^+$ state is dominated by the deformed head of a rotational band, is capable of describing some of the energy levels and electromagnetic decay rates for the low-lying positive parity states of $^{16}O$. The intensity of the deformed component present in this description of the ground state is similar to that predicted by Brown and Green. This model was extended by Bergstrom *et al.*,[8] who suggested that the deformation is triaxial. In the absence of internal excitation, the triaxial-rotor model of Davydov and Filippov[9] is then applicable to the deformed component and can accurately describe the positions of the $2_2^+$ state and a $3^+$ state at 11.08 MeV provided that the degree of triaxiality is large,[8] $\gamma \approx 24°$. The $2_2^+$ state predicted by this model has a predominantly $K=2$ character.[9] The electron scattering data then available were insufficient to determine the shape of the deformed component. Although a qualitative description of the electron scattering data was obtained by Bergstrom *et al.*, the assumptions concerning the deformed component were too restrictive to permit an accurate representation of the data.[8,10]

More recent experimental data have, to some degree, altered the selection of states which should belong to each of these models. For models, such as that of Brown and Green, in which parameters are adjusted to reproduce the energy levels of those states believed to belong to the model, this alteration affects their quantitative predictions. The recent $^{12}C(\alpha,\alpha_{i=0,1,2})$ and $^{12}C(\alpha,p_0)$ measurements of Ames[11] have clarified the spectrum of $^{16}O$ above 14 MeV. From these and earlier data he has suggested an alternative organization of states into collective bands based upon a core-excitation model. This model is basically a molecular model consisting of an alpha particle plus a $^{12}C$ core. Parent levels based upon the ground state of the $^{12}C$ core include the observed $K=0^+$ and $K=0^-$ rotational bands. The core may exist in excited states, which include the lowest $2^+$, $0^+$, and $3^-$ states of $^{12}C$. In the simplest weak-coupling version of this molecular model, the energy of a core-excited state is simply the energy of the parent state plus the energy of the $^{12}C$ excitation. The angular momentum is the vector sum of the parent and core angular momenta. On the basis of energetics, multipolarities, and resonance widths in the $^{12}C(\alpha,\alpha_i)$ reactions, Ames assigns many levels to collective bands. Some of the energy levels of this model are compared to the states we measured in Fig. 1, which also defines our nomenclature. The observed splitting between members of each multiplet suggests that the residual interaction is weak. This model accounts neatly for most of the positive parity states we have observed. The $4_3^+$ state at 13.87 MeV appears to display the largest splitting.

The molecular model of $^{16}O$ has recently received considerable theoretical attention. The work of Suzuki *et al.*[12–14] includes antisymmetrization and is not restricted to weak coupling. This work reproduces spectroscopic properties such as energy levels, electromagnetic transition

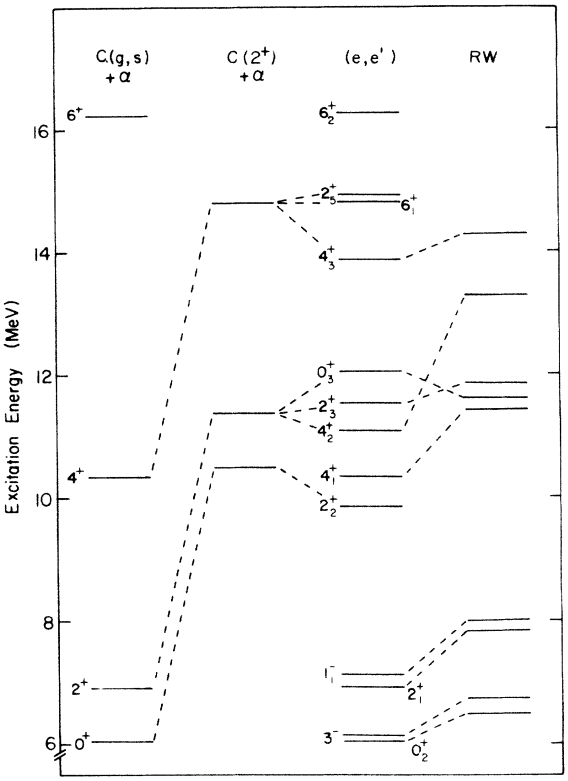


FIG. 1. The energy levels of states observed in the present (e,e') experiment are compared with the core-excitation model and with the shell-model calculation of Reehal and Wildenthal (RW).

rates, and $\alpha$-decay widths for nearly all isoscalar states below 15 MeV. In particular, the $4_3^+$ state is predicted to occur at 13.93 MeV and is described as an admixture of components based upon the ground state of $^{12}C$ and upon the first $2^+$ core excitation.[12]

There also has been renewed interest in the alpha-cluster model, which attempts to describe the states of $^{16}O$ by the configurations of either spherical or deformed alpha particles.[15,16] Some predictions of Robson's deformed alpha-cluster model,[17] assuming a tetrahedral ground-state configuration, will be compared with our data. The more recent work of Bauhoff *et al.*[18] successfully reproduces most of the isoscalar levels of $^{16}O$ below 15 MeV. Their approach differs from most earlier studies in that the customary restriction of the variational space to cluster positions with presupposed symmetries is removed. The organization of states into collective bands differs somewhat from that of other models.

On a more microscopic level, we must also consider shell-model descriptions of $^{16}O$. The fact that 4p4h excitations play a large role in the low-lying states of $^{16}O$ places impractical demands upon straightforward shell-model calculations. Although practical calculations must be truncated, no single truncation scheme is likely to successfully reproduce the properties of all physical states. Of the many calculations that have been attempted, it suffices for our purposes to cite three examples. The classic Zuker, Buck, and McGrory[19] truncation of the shell model space to the $1p_{1/2}$, $1d_{5/2}$, and $2s_{1/2}$ orbitals has

been reexamined, by Reehal and Wildenthal,[20] using an empirical residual interaction adjusted to reproduce selected energy levels in the $A=13$–22 region. Their predicted energy levels are also shown in Fig. 1. This approach adequately reproduces the positions of all states below about 14 MeV except the $2_2^+$ state at 9.85 MeV, which is attributed to a dominant $d_{3/2}^2$ or $p_{3/2}^{-2}$ configuration.[20] These configurations are beyond the scope of the model. Another scheme is provided by the weak-coupling model,[21] which is based upon the hypothesis that correlations between particles or holes within the same major shell dominate. This model can then afford to retain the entire $1p$ and $1d2s$ shells and is able to describe the $2_2^+$ state. Finally, in a third truncation scheme, Amos *et al.*[22] allowed 2p2h excitations within a model space including all orbitals up to, and including, $1f_{5/2}$. Their results indicate that the $2p1f$ shell makes important contributions to the 2p2h states near 11 MeV.

The assignment of physical states to collective bands or to model spaces is necessarily model dependent. Many of the models presently available have achieved a considerable degree of success in reproducing energy levels, electromagnetic transition rates, alpha decay widths, and the abundant qualitative spectroscopic information provided by transfer reactions. A more critical and discriminating evaluation of the structure models may now be made using the transition densities we have measured with high precision.

We report data for the electroexcitation of low-lying normal-parity states of $^{16}$O. Specifically, we report results for the two $0^+$ states at 6.049 and 12.049 MeV, the three $2^+$ states at 6.917, 9.845, and 11.52 MeV, the two $4^+$ states at 10.356 and 11.097 MeV, the $3^-$ state at 6.130 MeV, and the $1^-$ state at 7.117 MeV. The measurements were performed primarily at scattering angles of 90° and 160° and span momentum transfers between 0.6 and 2.6 fm$^{-1}$. A few low-$q$ points were taken at 45° and 60°. The $4^+$ state at 11.1 MeV has been observed with electron scattering for the first time. The diffraction minima and second maxima of the $0_2^+$ (6.05 MeV), $0_3^+$ (12.05 MeV), $2_1^+$ (6.92 MeV), and $2_3^+$ (11.52 MeV) states are clearly defined. The results of earlier experiments have been renormalized, as appropriate, to a recent analysis[23,24] of the elastic scattering from $^{16}$O. Radial transition charge densities were then extracted from this combined data set. Data for the $2_1^-$ state at 8.87 MeV and for states above 12 MeV will be reported in a later publication.[25]

The electroexcitation of discrete nuclear states is briefly reviewed in Sec. II. The experiment is described in Sec. III. The data analysis procedure, including some innovative line shape analysis techniques, is described in Sec. IV. The data and the extracted transition charge densities are presented in Sec. V. The predictions of several theoretical models of the structure of $^{16}$O are compared with the data in Sec. VI. Finally, our conclusions are presented in Sec. VII.

## II. ELECTRON SCATTERING

The plane-wave Born approximation (PWBA) to the unpolarized cross section for the electroexcitation of a nucleus from a state of angular momentum $J_i$ to a state of angular momentum $J_f$ can be written in terms of longitudinal and transverse contributions as:[26]

$$\left.\frac{d\sigma}{d\Omega}\right|_{\rm PWBA}=\eta\sigma_{\rm Mott}Z^2\left[\frac{q_\mu^4}{q^4}|F^L(q)|^2+\left[\frac{1}{2}\frac{|q_\mu^2|}{q^2}+\tan^2\frac{\theta}{2}\right]|F^T(q)|^2\right], \tag{1}$$

where $q^2$ and $q_\mu^2$ are the squares of the three- and four-momentum transfers, respectively, $Z$ is the atomic number of the target nucleus, and $\theta$ is the scattering angle. The point-charge cross section is given by

$$\sigma_{\rm Mott}=\left[\frac{\alpha}{2E_0}\right]^2\frac{\cos^2(\theta/2)}{\sin^4(\theta/2)}, \tag{2}$$

where $E_0$ is the incident energy and $\alpha$ is the fine structure constant. The density of final states factor is

$$\eta=\left[1-\frac{k_f-k_i\cos\theta}{E_T}\right]^{-1}, \tag{3}$$

where $k_f$ ($k_i$) is the exit (incident) electron momentum and $E_T$ is the total energy (including rest mass) of the recoil nucleus. Factors of $\hbar$ and $c$ have been suppressed. The structure information is contained in the longitudinal and transverse form factors $F^L(q)$ and $F^T(q)$, respectively. In PWBA, as described in Ref. 26, the $J$th multipole $F_J^L(q)$ of the longitudinal form factor is related to the Fourier-Bessel transform of the transition charge density $\rho_J(r)$ by

$$F_J^L(q)=\frac{\sqrt{4\pi}}{Z}\frac{\hat{J}_f}{\hat{J}_i}\int dr\, r^2 j_J(qr)\rho_J(r), \tag{4}$$

where $\hat{x}=\sqrt{2x+1}$.

We define the reduced Coulombic transition probability as

$$B(CJ)=\frac{2J_f+1}{2J_i+1}M_{JJ}^2, \tag{5}$$

where the multipole matrix element $M_{\lambda J}$ is defined as

$$M_{\lambda J}=\int dr\, r^{\lambda+2+k}\rho_J(r), \qquad k=0 \text{ for } J>0, \quad =2 \text{ for } J=0. \tag{6}$$

The transition radius is defined as

$$R_{\rm tr}^2=\frac{M_{J+2,J}}{M_{J,J}}. \tag{7}$$

The plane-wave approximation represented by Eq. (1) does not account for the distortion of the incoming and outgoing waves by the Coulomb field of the target nucleus. The distortions due to the spherical component of the ground-state charge distribution are included in the

distorted-wave Born approximation (DWBA) actually used to interpret the data.[27]

To first order, the acceleration of the electron wave by the Coulomb field of the nucleus can also be partially accounted for by use of a local or effective momentum transfer[28,29]

$$|q_{\text{eff}}|/|q| \approx [1-V_c(r_e)/E_0] , \tag{8}$$

where $V_c(r)$ is approximated by the Coulomb field of a uniformly charged sphere with the same total charge $Ze$ and root-mean-square charge radius $(\langle r^2\rangle)^{1/2}$:

$$-\frac{1}{Ze^2}V_c(r)=\frac{1}{r} \quad \text{for } r>R$$
$$=\frac{3}{2R}-\frac{r^2}{2R^3} \quad \text{for } r<R , \tag{9}$$
$$R=(\tfrac{5}{3}\langle r^2\rangle)^{1/2} .$$

The potential $V_c(r_e)$ was evaluated at $r_e=(J+1)/q$, a location which approximates the innermost peak of the overlap between incoming and outgoing partial waves.[29] This effective momentum transfer $q_{\text{eff}}$ provides a better estimate of the momentum actually transferred during the nuclear scattering event than does the asymptotic momentum transfer $q$. It is used for representational purposes as well as a means of approximating distortion effects in a plane wave treatment.

## III. EXPERIMENTAL ARRANGEMENT

The present experiment was performed at the MIT-Bates Linear Accelerator.[30,31] The beam was dispersed by a bending magnet and then a $\pm 0.3\%$ energy bin was selected by an energy defining slit.[32] A momentum dispersed beam was focused on the target. The dispersion of the beam was matched to that of the high-resolution energy-loss spectrometer.[32] The solid angle was defined by horizontal and vertical slits at the entrance to the spectrometer. The maximum solid angle was 3.325 msr. The detector array consisted of a position sensitive vertical drift chamber (VDC) located at the approximate position of the focal surface, followed by a multiwire proportional chamber that measures the scattering angle, and by two Čerenkov detectors that provide particle identification and a time fiducial for the wire chamber drift time measurements.[31] Typically, the resolution was $\Delta p/p = (1-2)\times 10^{-4}$.

The beam current incident on the target was monitored continuously by a nonintercepting ferrite-core toroid located approximately 3 m upstream from the scattering chamber.[33] Average beam currents on target between 1 and 40 $\mu$A were used.

At a scattering angle of 90°, beam energies between 90 and 357 MeV were used to obtain momentum transfers between 0.6 and 2.6 fm$^{-1}$. At a scattering angle of 160°, incident energies between 105 and 229 MeV produced a range of momentum transfer from 1.0 to 2.3 fm$^{-1}$. At 154.4 MeV, measurements were made at scattering angles of 45° and 60°, yielding momentum transfers of 0.59 and 0.78 fm$^{-1}$.

The targets were beryllium oxide foils. The stoichiometric ratio of $^9$Be to $^{16}$O is 1:1. The thicknesses ranged between 22 and 38 mg/cm$^2$. Most exposures were repeated with thin $^9$Be foils for background identification. The targets were mounted in transmission geometry with the normal to the target bisecting the scattering angle.

The energy scale of the focal plane detectors was determined using the known energy spacings between peaks. The incident electron energy $E_0$ was calibrated using the differential recoil between peaks belonging to nuclei of different masses. The precision of the energy calibration was between 1 and 6 parts in $10^3$, with the larger uncertainty occurring at the lower energies.

The overall uniformity of the focal-plane detector efficiency was measured by varying the position of a set of strong peaks along the detector using the spectrometer magnetic field. The efficiency was generally constant within the statistics of the measurements. A correction for a smooth variation in efficiency was applied to the 285 MeV data at 90°. This particular data set showed a significant nonuniformity of detector efficiency. The ratios of the cross sections corresponding to the same state that appeared in the overlapping portions of two spectra measured in different exposures and at two different positions in the detector differed from unity by 10—35% depending on the position along the detector. These ratios for different states in $^{16}$O and $^9$Be were used to extract an efficiency correction function[34] for the 285 MeV data at 90°. All of the 285 MeV data were corrected for efficiency as a function of channel position. An additional $\pm 10\%$ uncertainty was added in quadrature to the total error of each cross section measured at this energy.

Occasionally, fluctuations in detector response of about 5—10% were observed over a range smaller than the resolution width. These irregularities in the response of the system were found to be caused by localized errors associated with the aberrative corrections applied to the spectrum.[35] However, these irregularities conserve the total number of counts and therefore have a negligible effect upon the extraction of cross sections for strong peaks. Because the widths of these fluctuations were small compared with the resolution width, their impact was reduced by line shape fitting. When the peaks of interest were small compared with the underlying background, spectra were accumulated at several locations on the detectors either by shifting the physical position of the detectors or by making small variations of the spectrometer field. The local fluctuations in efficiency were thereby averaged out of the composite spectrum constructed off-line.

The data were corrected for the fraction of good events which were not analyzable.[34] A dead time correction was applied for the following: (1) events not analyzed by the computer due to a high event rate; (2) multiple events occurring within the 300 nsec response time of the VDC delay line system; and (3) VDC events corrupted by background radiation or other noise in the chambers. To lowest order these corrections were uniform over the focal plane. This correction factor was typically about 1.05 and was never larger than 1.3.

## IV. DATA REDUCTION AND ANALYSIS

### A. Line shape analysis

Figure 2 shows a typical electron scattering spectrum observed in the present experiment. The solid curves indicate the best fit to the peaks observed in the spectrum. The measured spectra were analyzed using a general program for the line shape analysis of binary reaction spectra called ALLFIT.[36,37] The program is designed to fit, within a single framework, electron scattering, hadron scattering, charge exchange, or transfer reactions. For the present purposes, it suffices to describe the (e,e') line shape. The total line shape $F(\omega)$, as a function of the electron energy loss $\omega$, consists of a sum of contributions from the individual peaks $F_j(\omega)$ in the spectrum and the background $A_{bg}(\omega)$,

$$F(\omega)=\sum_j F_j(\omega)+A_{bg}(\omega)\ . \tag{10}$$

The physical model of the process states that the observed distribution $F_j(\omega)$ for each peak $j$ arises from the convolution of the intrinsic nuclear excitation function $I_j$, the apparatus resolution function $R_j$, and the radiative response function $T_j$, such that

$$F_j(\omega)=(R_j\otimes T_j\otimes I_j)(\omega)\ , \tag{11}$$

where $\otimes$ denotes a convolution operator. However, a peak whose decay width is negligible can be described by the product $R_j\otimes T_j$ alone. The convolutions are performed with fast Fourier transform techniques.[38]

Unless the decay width of a state is less than about one-fourth the system resolution, we must include the intrinsic excitation function of that state. The intrinsic line shape $I_j$ was represented as a Lorentzian,

$$I_j(E)=N_j\frac{2}{\pi}\frac{\bar{E}^2\Gamma_j}{(\bar{E}^2-\bar{P}_j^2)^2+\bar{E}^2\Gamma_j^2},\quad \bar{E}>0$$

$$=0,\quad \bar{E}<0\ , \tag{12}$$

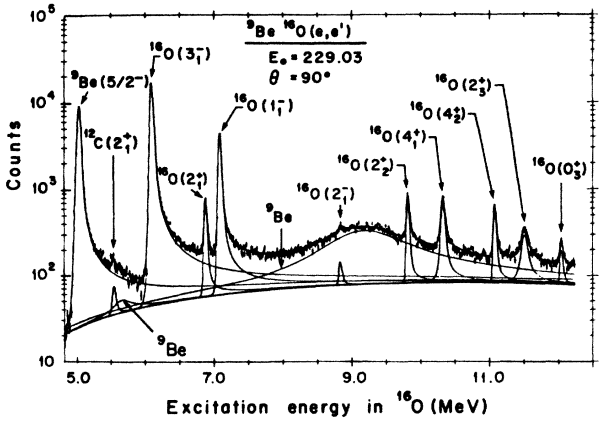


FIG. 2. Representative fitted electron scattering spectrum for BeO showing the total fitting function plus the contributions of individual peaks. This spectrum was collected in the minimum of the $0_2^+$ form factor.

where $N_j$ is the area and $\Gamma_j$ the full-width at half maximum (FWHM) of the resonance. The nuclear excitation energy $E(\omega)$ and the resonance position $P_j$ are referenced to the threshold $E_T$ for a hadronic decay using $\bar{E}=E(\omega)-E_T$ and $\bar{P}_j=P_j-E_T$, respectively. It was important to include the intrinsic widths of the $4_1^+$ and $2_3^+$ states in order to obtain accurate cross sections. Most of the low-lying states of $^9$Be also possess significant intrinsic widths and therefore constitute a complicated background under the $^{16}$O peaks of interest. An excellent description of this background was achieved by including the $^9$Be intrinsic line shapes explicitly.

Two methods were used to describe the resolution function and radiative response. In the first method, the convolution

$$L_I=R\otimes T \tag{13}$$

of the resolution function and the radiative response is represented by an empirical line shape.[34,37] A radiative correction is then applied as described by Maximon[39] and using the methods of Deady.[40] In the second method, the resolution function $R$ was represented by an empirical line shape $L_{II}$, while the radiative response $T$ was calculated theoretically following Mo and Tsai,[41] Bergstrom,[42] and Creswell[43] as described by Hyde-Wright.[37] When the data contain sufficient statistics and a strong isolated peak, it is more efficient to use the first method, although both methods agree. However, when the radiative tail at large electron-energy loss is not well determined by the data, more reliable results are obtained using the theoretical radiative response (the second method).

The total background function is represented by a piecewise continuous polynomial

$$A_{bg}(\omega)=\sum_{\lambda=0}^{3}\alpha_\lambda\omega^\lambda+\theta(\omega-\omega_T)\sum_{\lambda=1}^{3}\alpha'_\lambda(\omega-\omega_T)^\lambda\ , \tag{14}$$

where

$$\theta(\omega-\omega_T)=0\quad \omega<\omega_T$$

$$=1\quad \omega\geq\omega_T\ .$$

The electron energy loss corresponding to a decay threshold is $\omega_T$. In this experiment, using BeO targets, the first significant threshold occurs in $^9$Be at 1.665 MeV. The instrumental background was always quite small. Beyond the threshold for three-body breakup, the $^9$Be continuum contributes a substantial background below the $^{16}$O peaks.

The fitting criterion was the method of maximum likelihood, implemented for the Poisson distribution. The traditional chi-square ($\chi^2$) minimization procedure systematically underestimates small peak areas.[44] This underfitting can be especially severe in the presence of large backgrounds or large neighboring peaks. The correct fitting criterion for counting experiments must be based upon Poisson statistics.

The present algorithm, derived in Refs. 45 and 46, minimizes a quantity we call xi squared ($\Xi^2$), defined as

$$\Xi^2=2\sum_i\left[F(i)-y(i)-y(i)\ln\frac{F(i)}{y(i)}\right]\ , \tag{15}$$

where $y(i)$ is the number of counts observed in channel $i$ and $F(i)$ is the value of the fitting function at channel $i$. The minimization of $\Xi^2$ is equivalent to maximizing the likelihood for fits of experiments based upon the Poisson distribution. At the minimum of $\Xi^2$, the fitted area is equal to the observed area. There is no systematic underfit. The present minimization criterion has the virtues that the minimization function is non-negative and receives no contribution from $y(i)=F(i)$.

### B. Normalization of cross sections

The extracted cross sections for the $^{16}$O excited states presented in this paper were normalized to previous high quality absolute measurements[47,48] of elastic electron scattering from $^{16}$O. An accurate parametrization of the $^{16}$O ground state charge density has been generated from a combined analysis of these data.[24] This analysis included corrections for solid angle and target thickness. Tabulated results of this parametrization can be found in Ref. 23. A phase shift code[49] was used to calculate the $^{16}$O elastic cross section. The normalization factor obtained by this procedure is common to all peaks measured in a spectrum containing the elastic peak. It is important to note that the average agreement between the present absolute elastic scattering measurements and the calculations was better than ±5% for the 90° measurements, without any systematic energy dependence. At 160°, the scatter in the normalizations was about ±8%, consistent with the greater sensitivity to target orientation that is incurred at large scattering angles when using transmission geometry.

For each incident momentum, data were collected for several spectrometer field settings. Each setting covered a momentum bite of about 6% in $\Delta p/p$. Bites which did not include an elastic peak were normalized by comparing the region of overlap between successive momentum bites. After allowing for differing dead times, target thicknesses, or other experimental quantities affecting normalization, the normalizations required to obtain overall consistency usually differed from unity by less than ±5%. These correction factors were applied to the data and their statistical precision was folded into the experimental uncertainties.

### C. Discussion of uncertainties

The principal sources of uncertainty in the present measurements are the statistical and fitting errors and the normalization uncertainty. The normalization procedures liberate the present measurements from uncertainties in quantities such as solid angle, target thickness, charge integration, and dead time. The calculations of radiative effects were conducted in PWBA. The error resulting from this approximation was estimated to be less than 1%.

The fitting uncertainty in each peak area was obtained by standard error matrix techniques[44] and therefore includes contributions due to the uncertainty in each line shape parameter and its correlations with other parameters and with the background.

The statistical precision of the elastic peak contributes a normalization uncertainty between 0.4% and 4%. The uncertainty $\Delta E_0$ in the primary beam energy contributes a normalization uncertainty of about 2%, but this rises to about 5% near the diffraction minimum where the elastic cross section is most rapidly varying. The uncertainty in the scattering angle contributes a normalization uncertainty of less than 0.5%.

### D. The electroexcitation spectrum of $^{16}$O

The $^{16}$O states observed and included in the present analysis are shown in Fig. 1. Most spectra were divided into three energy regions. The first region contains all states below 9 MeV of excitation. The second region covers the excitation region between 9 and 12.5 MeV. The third region, above 12.5 MeV, will be discussed in detail in a forthcoming paper.[25,37] Each region was fitted independently. For each fit, the parameters of a resolution function for each nuclide ($^9$Be or $^{16}$O) were varied. The empirical tail parameters for all inelastic peaks were fixed to the values obtained from the fit to an isolated peak with sufficiently high statistics. The $^9$Be spectrum was represented by a sum of resonances plus a polynomial continuum and was explicitly included in the fit of the BeO spectrum. This procedure produced an accurate description of the background contributed by $^9$Be, thereby improving the accuracy of the fitted $^{16}$O peak areas.

Sample spectra are shown in Figs. 2 and 3. In Fig. 3 the $0_2^+$ and $3_1^-$ doublet near 6 MeV (80 keV separation) is shown fully resolved. However, at high momentum transfer the $0_2^+$ peak is very weak and only partially separated from the strong $3_1^-$ peak. In such cases, the line shape fitting to the spectrum was still able to extract the cross sections of the individual states separately. Since the separation of the $0_2^+$ and $3_1^-$ peaks is known with high precision, this separation was constrained whenever the $0_2^+$ peak was not strong enough to be easily distinguished from the $3_1^-$ peak. However, the overall position of this doublet was allowed to vary. The $(2_1^+, 1_1^-)$ doublet was completely resolved at all energies.

The intrinsic widths of the $4_1^+$ and $2_3^+$ states were comparable to the resolution of the present experiment. Neglecting the contribution of these intrinsic line shapes can produce cross section determinations as much as 50%

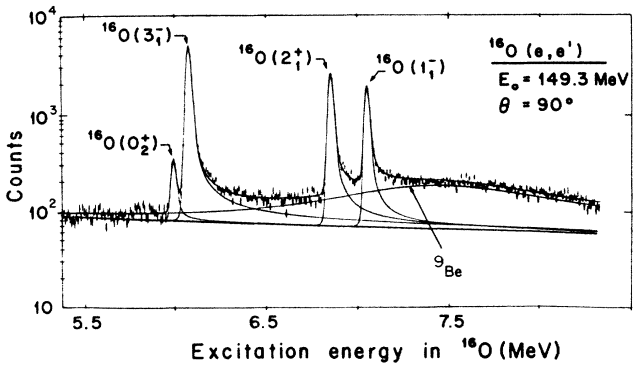


FIG. 3. Portion of a fitted electron scattering spectrum that illustrates the 80 keV separation between the $0_2^+$ and $3_1^-$ states.

too small because the intrinsic line shape blurs the distinction between background and peaks. The cross section data we report use the widths tabulated in Ref. 4.

The influence of the uncertainty in these widths was studied by fitting the $4_1^+$ and $2_3^+$ widths to our electron scattering data. The resulting width for the $2_3^+$ state was $69\pm2$ keV, which is in agreement with the tabulated width of $74\pm4$ keV.[4] The width we obtained for the $4_1^+$ state was consistent with, though considerably less precise, than the tabulated width of $25\pm4$ keV. As a measure of the sensitivity of the cross sections to the widths, the $2_3^+$ state was also reanalyzed using the narrower 69 keV width. This reanalysis produced cross sections for the $2_3^+$ state systematically smaller by 2%, a difference which we do not consider significant.

Allowance was made in the fitting procedure for the $1_2^-$ level at 9.63 MeV excitation, since this broad level influences the determination of the polynomial background and therefore also the areas of the adjacent $2_2^+$ and $4_1^+$ levels. The separation of this broad state from the $2_2^+$ peak at 9.85 MeV was kept constant in performing the line shape fit. A Lorentzian form of width $\Gamma=400$ keV was used for the $1_2^-$ intrinsic line shape. However, reliable measurements could not be obtained for this state. The $^{16}O$ levels at 11.26 and 11.62 MeV have large particle emission widths. No explicit evidence of these peaks was found. Their excitation strength was included implicitly in the polynomial background.

## V. EXPERIMENTAL RESULTS AND DISCUSSION

### A. Measured form factors

The differential cross sections for all states measured in this experiment can be obtained from the Physics Auxiliary Publication Service (PAPS).[50] Their form factors are

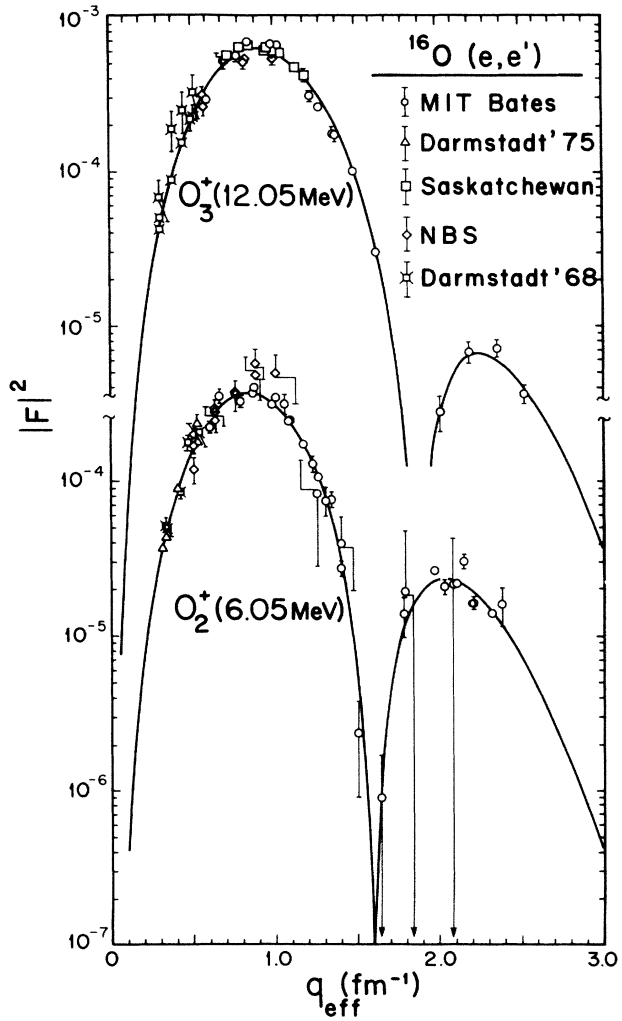


FIG. 4. The fitted monopole form factors are compared with data sets drawn from Darmstadt (Refs. 58 and 55), Saskatchewan (Ref. 57), NBS (Refs. 8 and 56), and MIT (the present work). Plane-wave results are plotted.

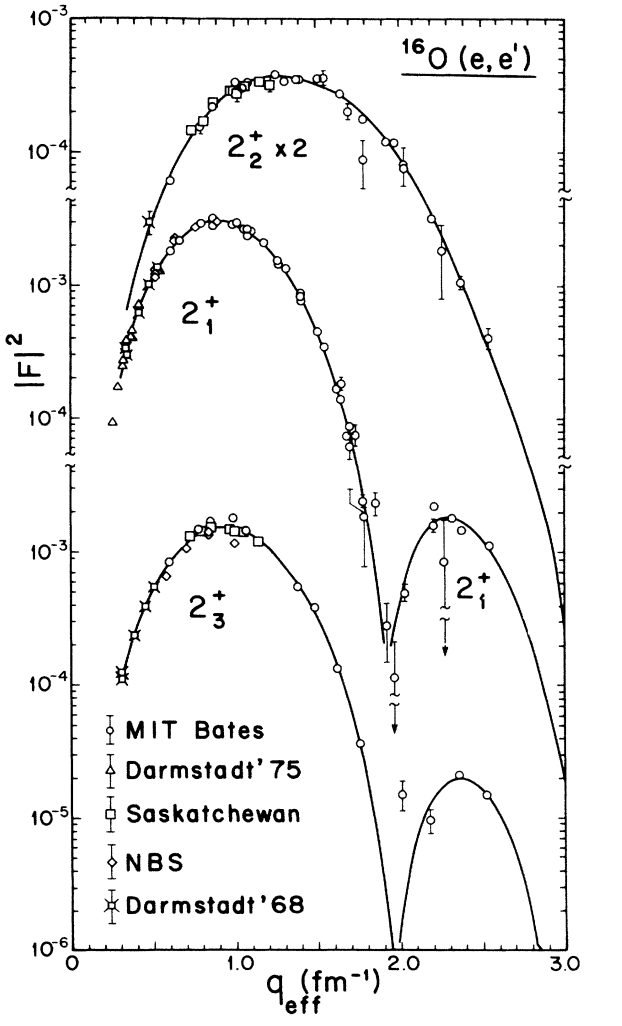


FIG. 5. The fitted $2^+$ form factors are compared with data sets drawn from Darmstadt (Refs. 58 and 55), Saskatchewan (Refs. 10 and 57), NBS (Refs. 8 and 56), and MIT (the present work).

shown in Figs. 4–7. The total form factor is defined by

$$|F(q)|^2=\frac{d\sigma}{d\Omega}\frac{1}{\eta}\frac{1}{Z^2\sigma_{\text{Mott}}}, \tag{16}$$

where $\eta$ and $\sigma_{\text{Mott}}$ are as given in Sec. II. Most of the previously existing electron scattering data on $^{16}$O for these states are also displayed in the figures and are also on deposit with PAPS.[50] The solid curves represent the best fits to the data using a distorted wave analysis that will be discussed in detail in the next section.

In DWBA the form factor is a function of two variables, $E_0$ and $\theta$, whereas in PWBA it is a function only of $q_{\text{eff}}$. For the purposes of display, the data and calculations in Figs. 5–7 have been recalculated using the maximum incident energy $E_m$, as described in Ref. 51, and plotted as functions of the effective momentum transfer. This transformation allows us to plot the data as a function of the single parameter $q_{\text{eff}}$. The transformation is defined by

$$\frac{d\sigma^*}{d\Omega}(E_m,q_{\text{eff}})=\frac{\frac{d\sigma}{d\Omega}(E_m,q_{\text{eff}})_{\text{DWBA}}}{\frac{d\sigma}{d\Omega}(E_0,q_{\text{eff}})_{\text{DWBA}}}\times\frac{d\sigma}{d\Omega}(E_0,q_{\text{eff}})_{\text{expt}}, \tag{17}$$

where

$$\frac{d\sigma}{d\Omega}(E,q_{\text{eff}})_{\text{DWBA}}$$

is the DWBA cross section calculated from the best DWBA fit to the data, and $d\sigma^*/d\Omega$ is the recalculated cross section.

The distorted wave codes we used[52,53] do not provide for nuclear current densities except as required by the continuity equation and were thereby restricted to the

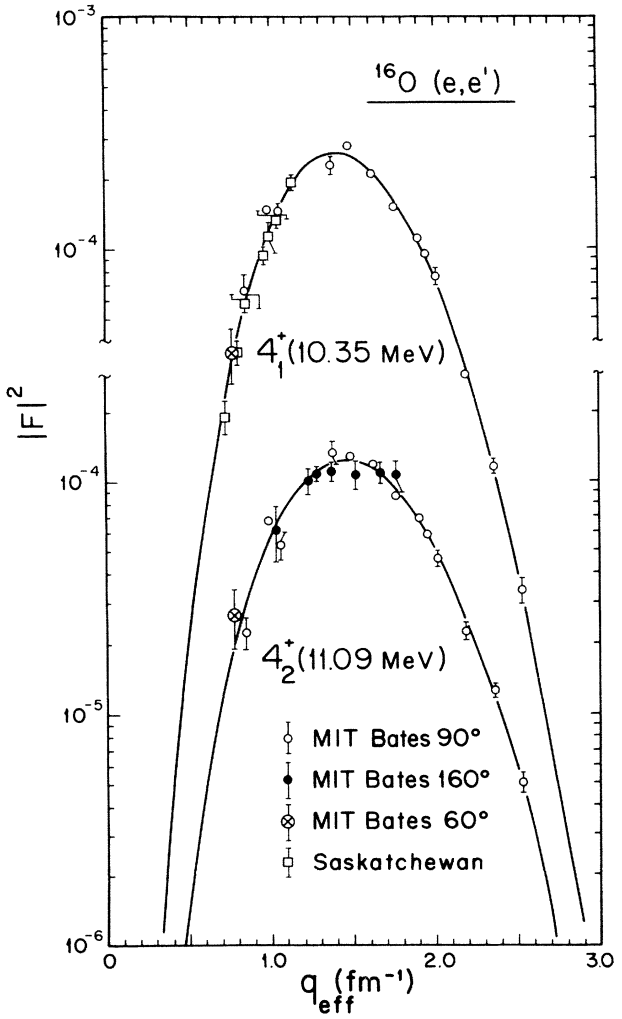


FIG. 6. The fitted $4^+$ form factors are compared with data sets drawn from MIT (the present work) and Saskatchewan (Ref. 10).

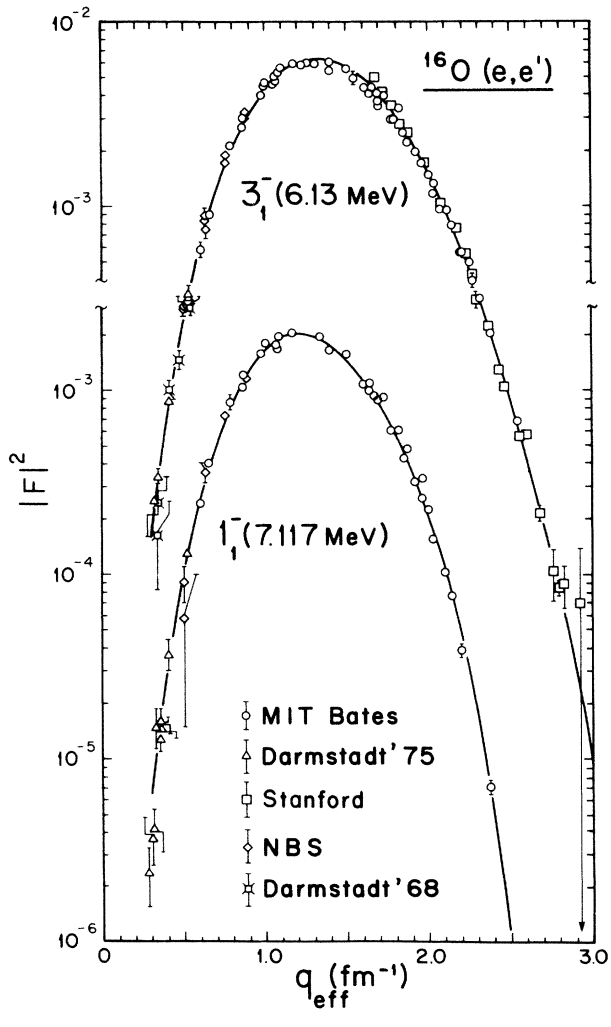


FIG. 7. The fitted $1^-$ and $3^-$ form factors are compared with data sets drawn from Darmstadt (Refs. 58, 59, and 55), Stanford (Ref. 54), NBS (Ref. 8), and MIT (the present work).

analysis of longitudinal form factors. In order to suppress any albeit small transverse contributions, the data collected at angles larger than 140° were omitted from the distorted wave analysis of the $1_1^-$, $4_1^+$, and $2_3^+$ states and are also omitted from Figs. 5–7. Only the $1_1^-$ state exhibits a significant transverse contribution. The longitudinal and transverse contributions were separated with a plane wave analysis to be described later.[37] The results are shown in Fig. 8.

The unresolved $3^+4^+$ doublet at 11.09 MeV has been observed for the first time with electron scattering. The 90° and 160° data are plotted together in Fig. 6. The absence of any systematic enhancement of the backward angle data demonstrates that the $3^+$ state, whose excitation must be entirely transverse, makes a negligible contribution to the observed peak. Therefore, we attribute the entire observed cross section to the $4_2^+$ state.

Most previously existing data for these states are included in the present analysis. The data sets we use are drawn from Refs. 8, 10, and 54–59. The data of Refs. 60–62 were omitted because of their larger relative errors. The data of Crannell[54] were normalized to elastic electron scattering from the proton and were not adjusted in the present analysis. The remaining experiments were all normalized to the elastic scattering from $^{16}O$, but used a variety of ground-state charge densities for this purpose. In the present analysis, all measurements relative to elastic scattering from $^{16}O$ were renormalized using the ground-state charge density of Miska *et al.*[24] Renormalizations as large as 7% were required. Therefore, this combined data set[50] should now be internally consistent.

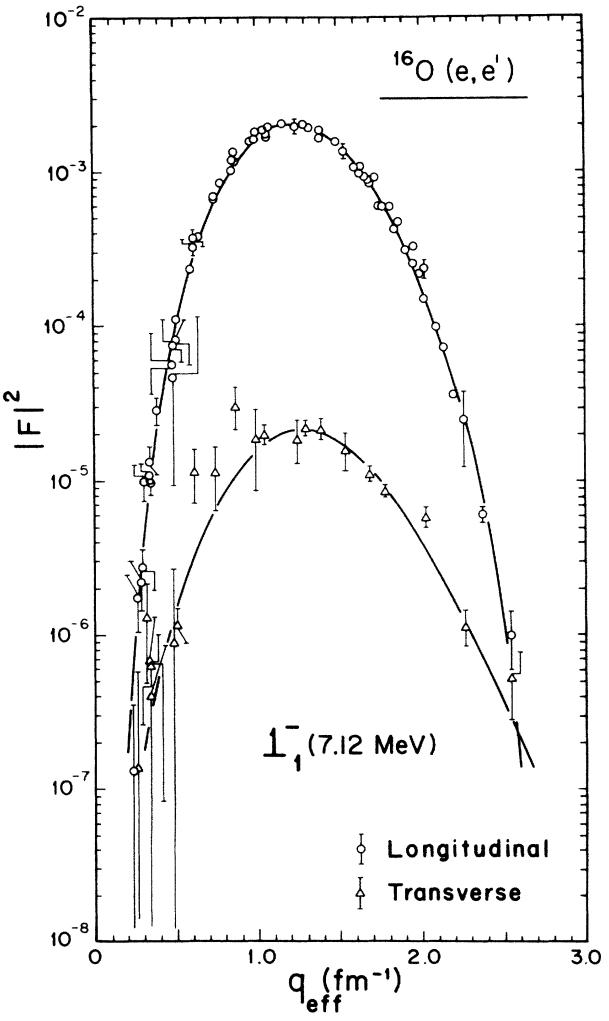


FIG. 8. Rosenbluth separation of the longitudinal and transverse contributions to the $1_1^-$ form factor.

The measurements of Crannell[54] provide data only for the $3_1^-$ state. The measurements of Stroetzel[55] were made at 117° and 165° and included the $0_2^+$, $0_3^+$, $2_1^+$, and $2_3^+$ states. In order to suppress the transverse contributions, the 165° data were not included in the analyses of $2^+$ states and are omitted from Fig. 5. Although the $1_1^-$ state was not resolved from the $2_1^+$ state, its contribution to the $2_1^+$ measurements at 117° is negligible for the range of momentum transfer reported by Stroetzel.[55] The data of Bergstrom *et al.*[8] and Miska *et al.*[58,59] cover the $0_2^+$, $3_1^-$, $2_1^+$, and $1_1^-$ states and are consistent with each other and with the present data wherever they overlap. The only earlier data on the $2_2^+$ and $4_1^+$ states were reported by Bergstrom *et al.*[10] and are consistent with the present measurements. The $2_3^+$ and $0_3^+$ data of Stroetzel,[55] Maruyama,[56] and Bergstrom and Auer[57] also are consistent with the present experiment where they overlap.

The longitudinal and transverse contributions to the $1_1^-$ form factor were separated using the plane-wave impulse approximation. Because $Z\alpha \ll 1$, this approximation is adequate for oxygen, provided that $q$ is interpreted as the local or effective momentum transfer. The separation was performed by fitting simultaneously the longitudinal and transverse contributions to the total form factor with the polynomial times Gaussian forms[37]

$$F_J^L(q)=\frac{\sqrt{4\pi}}{Z}\frac{q^J}{(2J+1)!!}e^{-y}\sum_\nu a_\nu y^\nu ,$$
$$F_J^T(q)=\frac{\sqrt{4\pi}}{Z}\left[\frac{J+1}{J}\right]^{1/2}\frac{\omega}{q}\frac{q^J}{(2J+1)!!}e^{-y}\sum_\nu b_\nu y^\nu , \tag{18}$$

where $y=(qb/2)^2$ and $b$ is an appropriate oscillator constant. This parametrization makes the long-wavelength limit explicit and is consistent with local charge conservation if we demand that the polynomial factors be equal at $q=0$, as we have done for the present fits. The expansion coefficients are tabulated in Table I.

This fit was used to construct experimental longitudinal and transverse data points. The longitudinal data points

TABLE I. Expansion parameters of the longitudinal and transverse form factors for the $1_1^-$ state, using $b=1.83$ fm.

| $n$ | Longitudinal $a_n$ (fm) | Transverse $b_n$ (fm) |
|---|---|---|
| 0 | −0.0162 | 0.0162 |
| 1 | 0.8999 | −0.8998 |
| 2 | −0.1478 | −0.7584 |
| 3 | | 0.1020 |

TABLE II. Fourier-Bessel expansion coefficients of the transition charge densities, using a cutoff radius $R = 8.0$ fm. The coefficients are in units of $10^{-4}$ fm$^{-3}$.

| $n$ | $0_2^+$ | $0_3^+$ | $2_1^+$ | $2_2^+$ | $2_3^+$ | $3_1^-$ | $4_1^+$ | $4_2^+$ |
|---|---|---|---|---|---|---|---|---|
| 1 | −7.821±0.11 | −8.974±0.13 | 73.808±0.24 | 11.613±0.17 | 50.471±0.28 | 99.542±0.34 | 26.944±0.36 | 18.734±0.38 |
| 2 | −65.306±1.36 | −82.744±1.06 | 158.471±0.71 | 45.090±0.50 | 119.461±0.97 | 303.073±0.92 | 69.711±0.90 | 48.585±0.66 |
| 3 | −98.481±4.59 | −147.279±3.65 | 108.520±0.60 | 75.207±0.93 | 95.774±1.30 | 402.446±0.74 | 75.343±0.68 | 58.699±0.56 |
| 4 | −3.982±8.66 | −100.967±6.44 | −0.544±1.12 | 72.319±0.78 | 7.200±2.80 | 293.928±0.77 | 43.729±0.98 | 41.808±1.09 |
| 5 | 100.648±9.14 | 21.704±6.09 | −55.323±1.08 | 36.950±1.24 | −58.751±1.84 | 125.227±1.01 | 13.465±3.21 | 17.953±3.44 |
| 6 | 97.778±9.31 | 83.182±6.87 | −34.005±6.19 | 13.428±4.35 | −35.584±8.41 | 32.413±4.38 | 3.114±6.56 | −3.434±7.61 |
| 7 | 56.790±41.14 | −9.535±31.21 | −5.508±13.46 | −0.250±6.71 | 13.435±16.93 | 4.905±12.15 | −1.504±4.62 | 0.890±5.46 |
| 8 | 9.046±73.24 | −0.713±44.78 | 1.143±10.56 | −0.112±4.65 | −4.283±12.08 | −0.450±10.42 | 0.620±3.16 | −0.272±3.74 |
| 9 | −10.910±47.42 | 0.376±37.85 | −0.181±7.49 | 0.070±3.18 | 1.488±8.34 | −0.229±7.47 | −0.254±2.17 | 0.093±2.58 |
| 10 | 2.986±59.85 | 0.248±26.64 | 0.021±5.24 | −0.032±2.19 | −0.556±5.78 | 0.210±5.25 | 0.107±1.52 | −0.035±1.80 |
| 11 | 1.102±47.82 | −0.952±19.07 | −0.023±3.68 | 0.014±1.54 | 0.221±4.06 | −0.125±3.72 | −0.047±1.08 | 0.014±1.28 |
| 12 | −2.317±44.33 | 3.769±18.80 | 0.019±2.62 | −0.006±1.09 | −0.092±2.89 | 0.067±2.66 | 0.021±0.77 | −0.006±0.92 |
| $M_{JJ}$ | 0.976±0.052 ($e$ fm$^2$) | 1.062±0.045 ($e$ fm$^2$) | 2.791±0.008 ($e$ fm$^2$) | 0.221±0.033 ($e$ fm$^2$) | 1.843±0.025 ($e$ fm$^2$) | 14.20 ±0.14 ($e$ fm$^3$) | 20.5 ±1.9 ($e$ fm$^4$) | 19.3 ±2.2 ($e$ fm$^4$) |
| $R_{tr}$ (fm) | | | 4.026±0.038 | 3.6 ±1.4 | 3.98 ±0.10 | 4.049±0.068 | 4.48 ±0.43 | 5.51 ±0.30 |
| $\chi_\nu^2$ | 1.6 | 1.9 | 5.7 | 1.6 | 4.7 | 12.7 | 2.8 | 2.1 |

were obtained by subtracting the fitted transverse contribution from the total measured form factor, suitably adjusting its error bar, and are plotted whenever the transverse contribution was less than 10% of the square of the total form factor. Similarly, transverse data points were obtained by subtracting the fitted longitudinal contribution and are plotted whenever the subtracted term was less than 90%.

The extracted longitudinal and transverse form factors for the $1_1^-$ state are displayed in Fig. 8. The solid curves represent the best plane-wave fit, which is seen to represent the data quite well over the entire range of momentum transfer. The magnitude of the transverse form factor is about 1% of the longitudinal at the maximum. This is the largest transverse form factor we have observed for this set of states.

### B. Transition densities

We have extracted transition charge densities in the distorted-wave approximation[63] using the code FOUBESØ (Ref. 52) for the monopole data and the code HADES (Ref. 53) for all other data. The high-$q$ properties of the fitted densities were biased using pseudodata generated within the upper-limit envelope,[64]

$$\rho_l(q) \lesssim \rho_l(q_m)(q_m/q)^4 h(q)/h(q_m) , \tag{19}$$

where $\rho_l(q)$ is the Fourier transform of the transition density, $q_m$ is the maximum experimental momentum transfer, and $h(q)$ is the dipole fit to the proton form factor.[26] This condition was derived by Dreher *et al.*[64] by requiring smoothness of the fitted densities, and is less restrictive than the exponential envelope employed in many similar analyses.[63]

All densities, except that for the $1_1^-$ state, were represented by the Fourier-Bessel expansion

$$\rho_l(r) = \sum_n a_n j_l(q_n r) \quad r < R$$
$$= 0 \quad r > R , \tag{20}$$

where

$$j_l(q_n R) = 0 .$$

The cutoff radius $R$ was chosen to be 8 fm. The expansion parameters are listed in Table II.

The presence of considerable low-$q$ data for many of these states suppresses oscillations in the fitted densities for a large radius. However, the fitted densities for a few of the states which lack such low-$q$ data exhibit small oscillations at large radii. In many similar analyses, these surface oscillations are suppressed artificially using an exponential large-$r$ tail bias.[63] However, this procedure is somewhat arbitrary and can produce an unrealistically small estimate of the uncertainty in the fitted matrix elements. Therefore, no tail constraints were imposed in the present analysis.

The Fourier-Bessel expansion is not well suited to describe the $1_1^-$ data for momentum transfers below 0.5 fm$^{-1}$. Isospin invariance produces an approximate selec-

tion rule which severely inhibits isoscalar dipole transitions near the photon point. These transitions occur only through isospin mixing or through the second term of the long-wavelength expansion. The contribution of each term of the Fourier-Bessel series to the form factor exhibits a moderate degree of localization in momentum transfer. Using the typical cutoff radius $R=8.0$ fm, the first term peaks at $q=0.57$ fm$^{-1}$, well above the lowest experimental momentum transfer. Unless the cutoff radius is increased beyond 12 fm, a $\chi^2$ fit to this data using the Fourier-Bessel expansion does not reproduce the suppression of the form factor at smaller momentum transfer. However, the use of such a large cutoff radius results in unreasonable oscillations in the density at large radius.

A more appropriate description of inhibited transitions is provided by an expansion whose form factor is a polynomial in $q$ times a Gaussian, similar to that employed in the plane-wave fit. Using HADES, the separated longitudinal data were fitted with a Laguerre expansion of the form

$$\rho_l(r)=x^l e^{-x^2}\sum_n c_n L_n^{l+(1/2)}(2x^2)\,, \tag{21}$$

where $x=r/b$ and $L_n^a(z)$ is a generalized Laguerre polynomial of the form

$$L_n^a(z)=\sum_{m=0}^{n}(-)^m\frac{\Gamma(a+n+1)}{\Gamma(n-m+1)\Gamma(a+m+1)}\frac{z^m}{m!}\,. \tag{22}$$

The expansion is complete for any $b$. We chose a value $b=1.80$ fm according to the harmonic oscillator model of the ground state. This expansion contains a contribution linear in $q$ that accurately reproduces the low-$q$ form factor. The Gaussian factor suppresses the density at large radius. The expansion parameters are given in Table III. The transition radius is unusually large because the matrix element $M_{JJ}$ is suppressed.

The best fits to the form factor data are displayed as solid curves in Figs. 4–7. It is clear from these figures that these parametrizations of the transition densities represent the global data sets quite well. There are no systematic discrepancies between data sets, partially as a result of our renormalization of earlier experiments to a common ground-state charge density. For some states large reduced $\chi^2$ values result from a small number of data points which deviate substantially from the rest of the data. These isolated inconsistencies have little impact upon fits to data sets as extensive as these. For example, rejecting 10% of the data for the $3_1^-$ state would reduce $\chi^2$ by a factor of 4. For most states, the $\chi^2$ per point contributed by the present experiment is about 2.0.

The fitted transition densities and their error envelopes are displayed in Figs. 9–12. The uncertainty in a fitted

TABLE III. Laguerre expansion of the $1_1^-$ transition charge density, using $b=1.80$ fm.

| $n$ | $c_n\times10^4$ (fm$^{-3}$) |
|---|---|
| 0 | 619.386 ±1.830 |
| 1 | 136.488 ±0.817 |
| 2 | −57.730 ±0.737 |
| 3 | 2.520 ±0.423 |
| 4 | 2.033 ±0.340 |
| 5 | 1.693 ±0.197 |
| 6 | −1.839 ±0.203 |
| 7 | 0.582 ±0.093 |
| $M_{JJ}$ | −0.0195±0.0019 $e$ fm |
| $R_{tr}$ | 16.48 ±0.63 fm |
| $\chi_v^2$ | 5.1 |

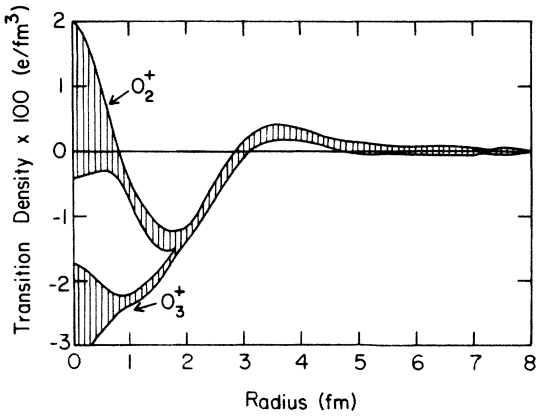


FIG. 9. Transition charge densities extracted for the $0^+$ states.

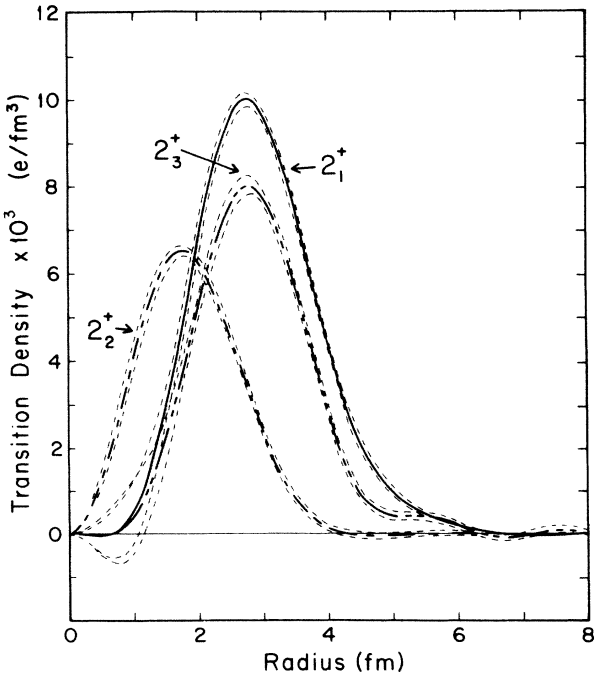


FIG. 10. Transition charge densities extracted for the $2^+$ states.

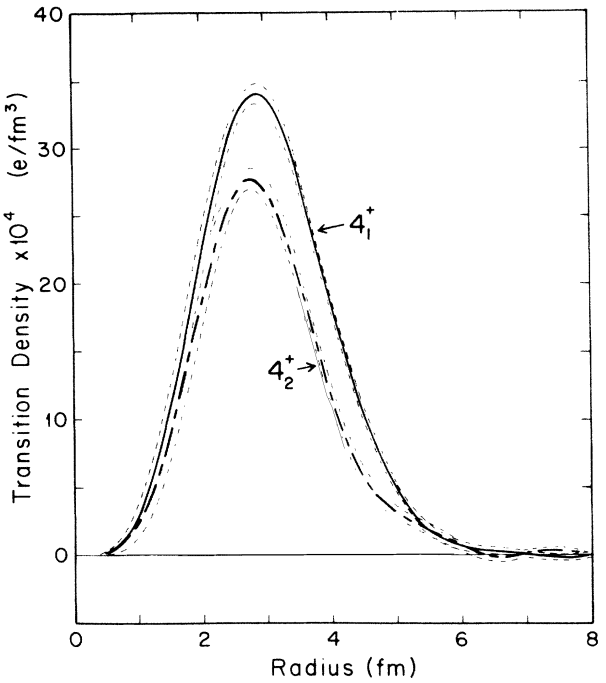


FIG. 11. Transition charge densities extracted for the $4^+$ states.

density contains two contributions. The statistical precision of the data contributes to the statistical error. The incomplete, or finite, range of momentum transfer spanned by the experiment contributes to the incompleteness error, estimated according to the methods of Dreher *et al.*[64] These two contributions are displayed separately

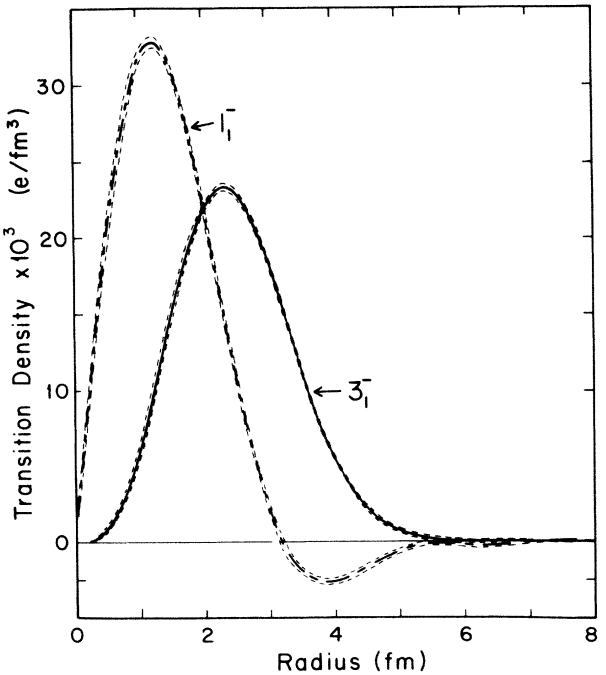


FIG. 12. Transition charge densities extracted for the $1^-$ and $3^-$ states.

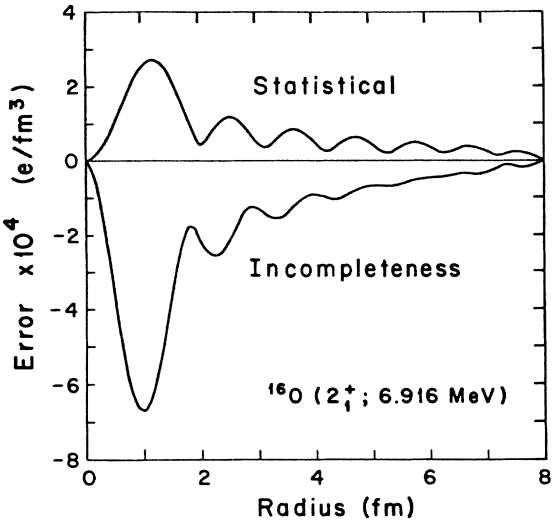


FIG. 13. The separate contributions of the statistical and incompleteness errors to the error band for the $2_1^+$ density. The incompleteness error has been inverted for clarity.

in Fig. 13 for the $2_1^+$ state. The incompleteness error tends to prevail. The relatively large uncertainties in the monopole densities at the origin are dominated by this incompleteness error.

The $0_2^+$ transition density has an interior peak at about 1.7 fm and a surface lobe at about 3.5 fm, consistent with our qualitative expectations for the motion of a 4p4h or $\alpha$-cluster configuration. The $0_3^+$ transition density, on the other hand, displays the dominant central lobe expected whenever the $s$ shells participate. This is consistent with the identification of this state with a dominant 2p2h configuration.

One striking feature of our measured quadrupole densities is the contrast between the densities of the $2_2^+$ state and those of the $2_1^+$ and $2_3^+$ states—the $2_2^+$ density peaks at a considerably smaller radius. Several qualitative interpretations are consistent with this observation. Several shell-model calculations suggest that this transition proceeds primarily between hole states in the $p$ shell.[20,21] Alternatively, the core-excitation model suggests that this state consists primarily of a $2^+$ core excitation coupled to an $\alpha$ particle in a $0^+$ state of relative motion.[11] Both of these interpretations suggest that the form factor for excitation of the $2_2^+$ state of $^{16}$O should be similar in shape to that of the $2_1^+$ state of $^{12}$C, as in fact is observed.[54,65] Finally, we can associate the $2_1^+$ state with the predominantly $K=0$ member and the $2_2^+$ state with the predominantly $K=2$ member of a rotational band based upon a triaxially-deformed intrinsic state. The $K=2$ member has a smaller moment of inertia, and hence greater energy, than does the $K=0$ member.

The $4^+$ transition densities are compared in Fig. 11. These represent the first charge density measurements for the second $4^+$ state. These states have similar strengths and shapes.

The negative-parity transition densities are displayed in Fig. 12. Both densities are very well determined by the

data. The abundant low-$q$ data are sufficient to suppress oscillations at large radii and to measure the geometric moments of these distributions accurately.

## VI. COMPARISON WITH STRUCTURE MODELS

A comprehensive review of the vast literature pertaining to the nuclear structure of $^{16}O$ is beyond the scope of the present paper. Rather, in the hopes of obtaining new insight into these structure questions, we compare our data with the predictions of several representative structure models. It is sufficient, for our purposes, to compute the theoretical form factors in the plane-wave approximation, including nucleon and center-of-mass form factors as described in Ref. 23. All model calculations use the radial parameters proposed by the original authors.

The $0^+$, $2^+$, and $4^+$ form factors are compared with the models described in the following subsections A—C in Figs. 14, 16, and 18, respectively. The transition densities are compared in Figs. 15, 17, and 19. The model calculations are illustrated with a legend common to this set of

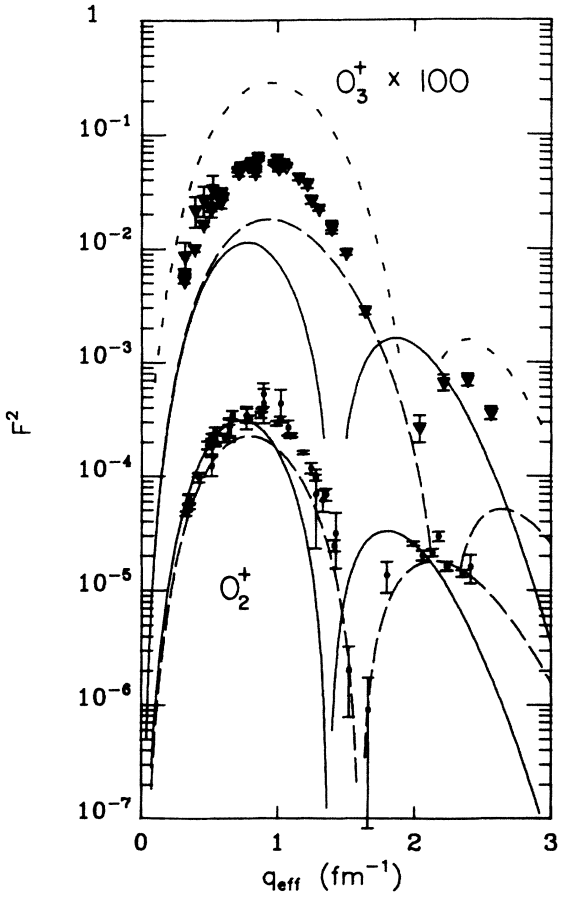


FIG. 14. Comparison between the experimental $0^+$ form factors and the predictions of the Brown-Green (solid lines), weak-coupling (long-dashed lines), and Amos (short-dashed lines) models. Data points whose relative uncertainties are near 100% have been suppressed for clarity.

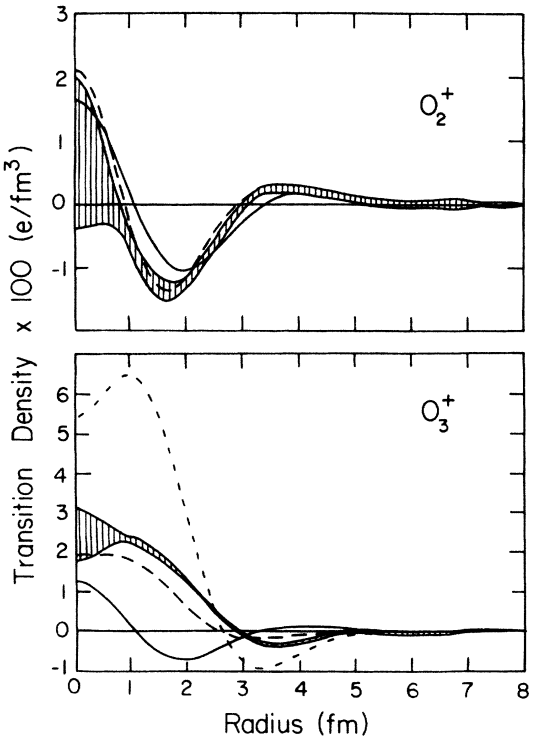


FIG. 15. Comparison between the experimental $0^+$ transition densities (shaded bands) and several models (same legend as Fig. 14).

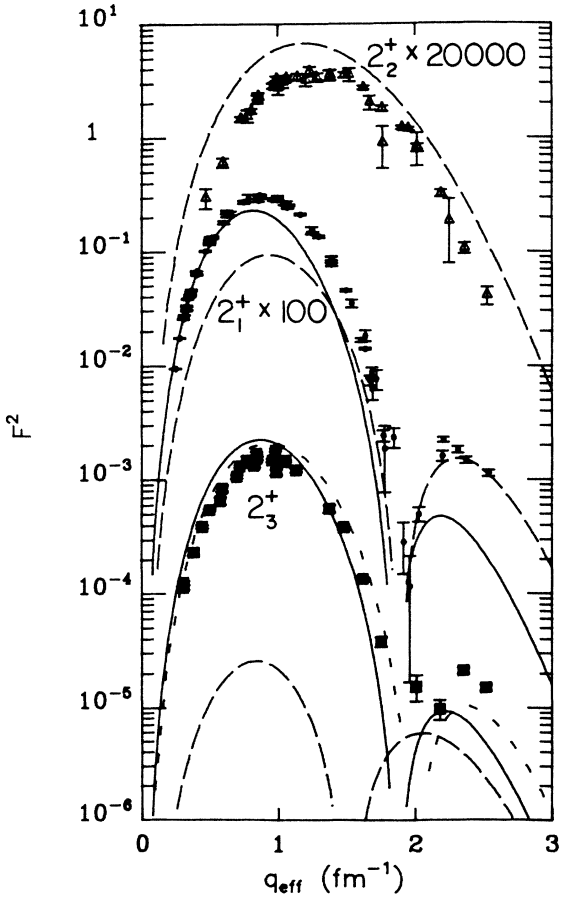


FIG. 16. Comparison between the experimental $2^+$ form factors and several models (same legend as Fig. 14).

figures. The relative signs of the experimental densities displayed in these figures were chosen according to the model calculations.

### A. Brown-Green model

An early coexistence model of the structure of $^{16}O$ was constructed by Brown and Green,[5,6] who postulated the existence of 0p0h, 2p2h, and 4p4h deformed states. The equilibrium deformations were based upon Refs. 66 and 67, which reported energy minima near deformation parameters $\beta=0.3$ and $\beta=0.5$ for 2p2h and 4p4h configurations, respectively. Nilsson orbitals and a semirealistic two-body residual interaction were used. The unperturbed energy of each model configuration was adjusted to fit the measured energy spectrum, assigning physical states to model states according to the best experimental information available at that time. Erikson[68,69] has calculated the electromagnetic form factors predicted by this model.

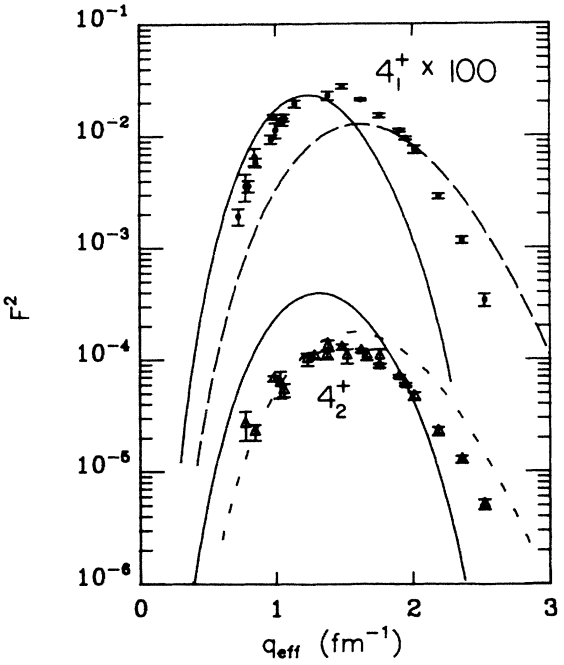


FIG. 18. Comparison between the experimental $4^+$ form factors and several models (same legend as Fig. 14).

The original Brown-Green (BG) model was based upon the assumption that the third monopole state produced by the model is to be identified with a very broad, and tentative, level at 11.26 MeV. The actual existence of this state is open to question.[70,71] Erikson has adjusted the model using the narrow $0^+$ state at 12.05 MeV that we have ob-

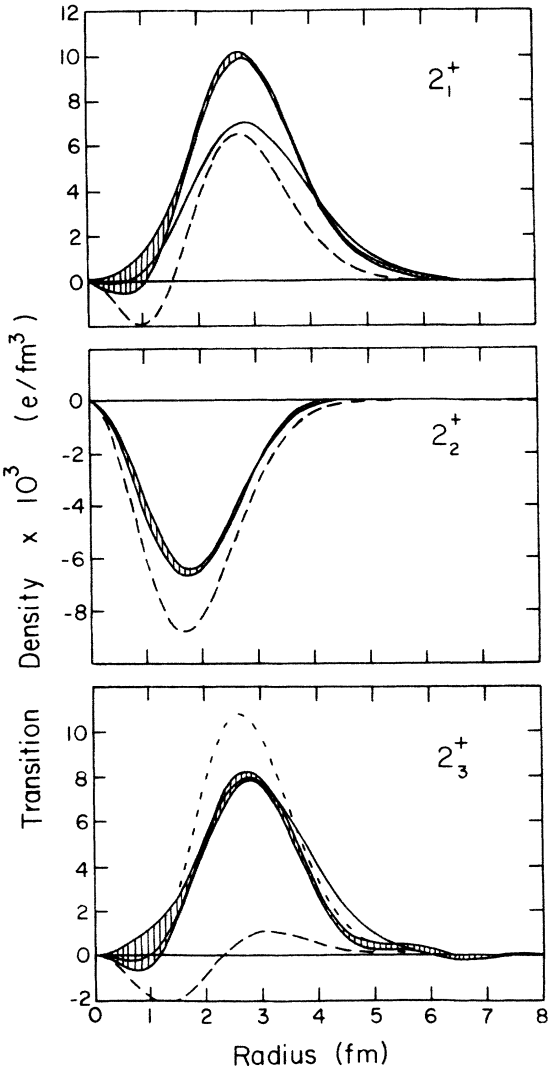


FIG. 17. Comparison between the experimental $2^+$ transition densities and several models (same legend as Fig. 15).

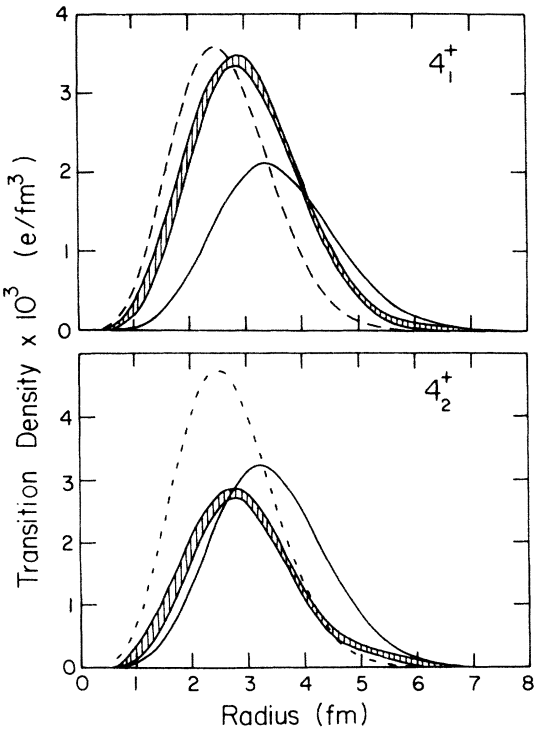


FIG. 19. Comparison between the experimental $4^+$ transition densities and several models (same legend as Fig. 15).

served. The present comparisons are based upon this small adjustment. A single radial scale parameter was fitted by Erikson to the elastic scattering data.[68]

The predicted monopole form factors are compared with the data in Fig. 14. The transition densities are compared in Fig. 15. The $0_2^+$ form factor obtained in a spherical limit is illustrated in Fig. 20. The BG model is moderately successful in reproducing the $0_2^+$ transition density and form factor. It is clear that the strong degree of deformation postulated by the model is required to obtain the observed strength without the empirical renormalization customarily required by shell-model calculations. The deformation is equally important to the strength of all multipolarities.

The form factor predicted for the $0_3^+$ state is much weaker than that observed. Moreover, the transition densities have qualitatively dissimilar shapes. The origin of these discrepancies is not clear at the present time. Perhaps the identification of the observed state with the model state is invalid. However, monopole form factors are second-order effects in this model and depend upon delicate cancellations between much larger contributions.[68] Therefore, we cannot expect quantitative accuracy from this model, especially without a more realistic treatment of the radial wave functions.

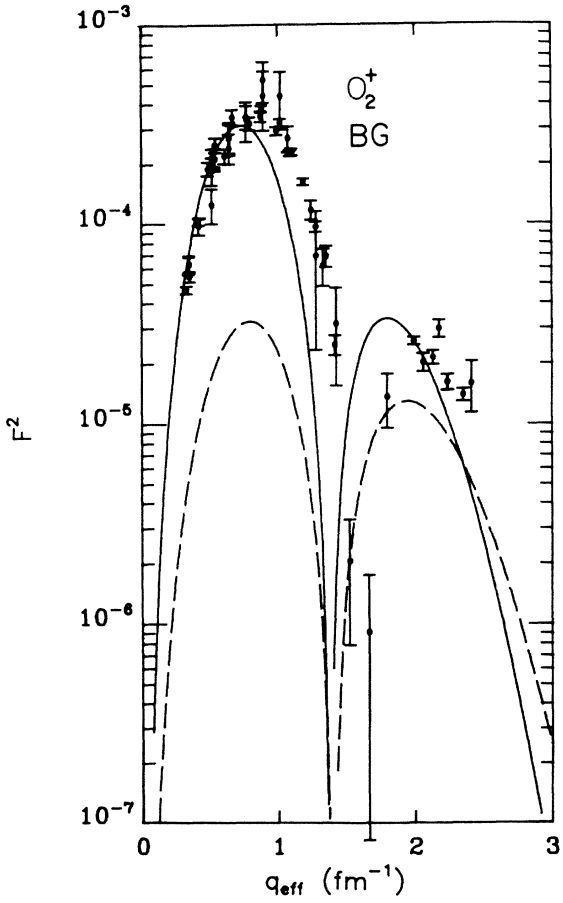


FIG. 20. The Brown-Green $0_2^+$ form factor (solid line) and its spherical limit (dashed line) are compared with the data.

The predictions of the BG model for the $2_1^+$ and $2_3^+$ states are compared with the data in Fig. 16. The theoretical and experimental transition densities are compared in Fig. 17. The level of agreement is remarkable considering the limitations of the model. At the maxima of the form factors, the $2_1^+$ is somewhat underpredicted while the $2_3^+$ is somewhat overpredicted. Neither theoretical form factor has sufficient strength at larger momentum transfer. Erikson speculated that near-perfect agreement between the model and the data then available might possibly be obtained from a relatively minor adjustment of the residual interaction.[68] This speculation still appears tenable on the basis of the present more extensive data set.

The original BG model states were constructed by assuming that the $4^+$ state at 16.8 MeV corresponds to the predominantly 2p2h model state.[5] Due to the large energy spacing of the unperturbed configurations assumed by the model, the calculated states are almost pure configurations, with the predominantly 4p4h state occurring at lower excitation energy. However, the present experiment failed to detect a strong $4^+$ state near 16.8 MeV. The only strong $4^+$ states observed above the $4_1^+$ state were the $4_2^+$ and $4_3^+$ states at 11.1 and 13.87 MeV, respectively. The form factors for these three states are similar in both shape and magnitude.[37] The data for the $4_3^+$ state will be reported in a later publication.[25]

There is strong experimental evidence that the $4_2^+$ state is predominantly 2p2h in character. This state is the most strongly populated $4^+$ state in the two-particle (2p) transfer reaction $^{14}N(\alpha,d)$ at $E_\alpha = 20$–$40$ MeV.[72,73] It is, in fact, one of the strongest states of any multipolarity. On the other hand, this state is only weakly populated[74] by the 4p transfer $^{12}C(^6Li,d)$. The $4_1^+$ state produces a strong resonance in the elastic scattering of $\alpha$ particles[1,11] by $^{12}C$ and is strongly populated by 4p-transfer reactions,[74] but is weakly populated by 2p transfer. The $4_3^+$ state is relatively weakly excited by both 2p and 4p transfer and, therefore, probably has a more complicated structure.

These observations suggest that the dominantly 4p4h state should be identified with the $4_1^+$ state, while the dominantly 2p2h state should be identified with the $4_2^+$ state at only 11.09 MeV. Reducing the energy difference between the physical states by this large amount will greatly enhance the configuration mixing that would be present in a revised version of the BG model.

The $4^+$ form factors predicted by the BG model are compared in Fig. 18 to the data for the $4_1^+$ and $4_2^+$ states at 10.35 and 11.09 MeV. The transition densities are shown in Fig. 19. The 2p2h form factor is considerably stronger because the 2p2h ground-state amplitude is larger. It is apparent from the data that considerably greater mixing of these amplitudes is required if the model is to reproduce the data for the $4^+$ states. An increased 2p2h amplitude in the lowest state would enhance the $4_1^+$ density, as required, and correspondingly reduce the form factor of the orthogonal model state, presumably the $4_2^+$ state. However, because the predicted radial shapes of both configurations are so similar, this modification alone is not sufficient to reproduce the data. The radial shapes must also be modified.

One possible reason for the failure of the BG model to describe the $0_3^+$ state and for its difficulties in describing the radial shapes of the $4^+$ states is its assumption of axial symmetry. Triaxial deformation of the nonspherical components of this model may produce radial shapes in better agreement with the data. To evaluate the assumption of axial symmetry, it is also important to calculate the radial transition densities the model predicts for the $K=2$ band, which presumably includes the $2_2^+$ state.[68] Perhaps the $4_3^+$ state is also of this nature. Clearly, further development of the model is required before it can be evaluated definitively.

The negative parity states of good angular momentum are projected from 1p1h and 3p3h excitations of the Brown-Green ground state. The longitudinal form factors for several of the $K=1$ states have been computed by Erikson.[69] These results are compared with the $1_1^-$ and $3_1^-$ form factors in Fig. 21. Erikson also has estimated the importance of 1p1h excitations spanning $3\hbar\omega$ by calculating the admixture of $3\hbar\omega$ components introduced into pure 1p1h basis states by a suitable residual interaction. These admixtures were used to estimate correction factors applied to the form factors of the actual model states. This estimation procedure suggests that the $3\hbar\omega$ contributions are substantial and improve the agreement with the data. The form factor predictions are in reasonable agreement with the data, but the radial scale is compressed.

### B. The weak-coupling model

The weak-coupling model[21] is a variation of the spherical shell model based upon excitations from the $1p$ shell into the $2s1d$ shell. The defining hypothesis of this model is that correlations between particles or between holes within the same major shell dominate. The eigenvalue problems for $n_1$ particles in the $2s1d$ shell or $n_2$ holes in the $1p$ shell are solved separately, producing the basis within which a weak residual interaction is diagonalized. This model was developed by Ellis and Engeland[21] and was later used by Horsfjord[75] to compute electromagnetic form factors for some of the positive parity states of $^{16}$O. The form factors for states with $J>0$ employed oscillator wave functions with $b=1.70$ fm. The monopole densities employed Woods-Saxon wave functions as prescribed by Horsfjord. Configurations outside this model space were included, very approximately, in a constant polarization charge $\delta e_p=\delta e_n=0.5e$.

The weak-coupling model (WCM) predictions for the monopole form factors are shown in Fig. 14. The WCM radial densities are compared with the experimental densities in Fig. 15. The model density for the $0_2^+$ state is in relatively good agreement with experiment. The predicted $0_3^+$ density is systematically low and the node occurs at a radius that is slightly too small.

Relatively small perturbations of the radial density can produce dramatic effects upon a monopole form factor at moderate momentum transfer. The $0_2^+$ form factors calculated using Woods-Saxon and harmonic oscillator wave functions[75] are compared in Fig. 22. The large sensitivity

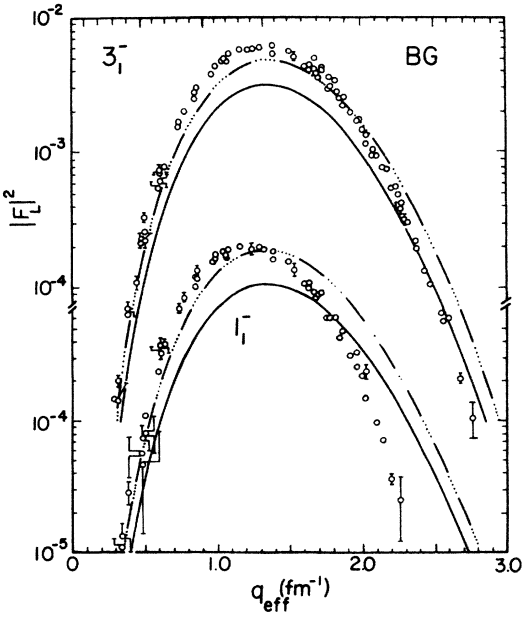


FIG. 21. Comparison between the $1^-$ and $3^-$ data and the Brown-Green model with (dash-dot lines) and without (solid lines) a $3\hbar\omega$ contribution.

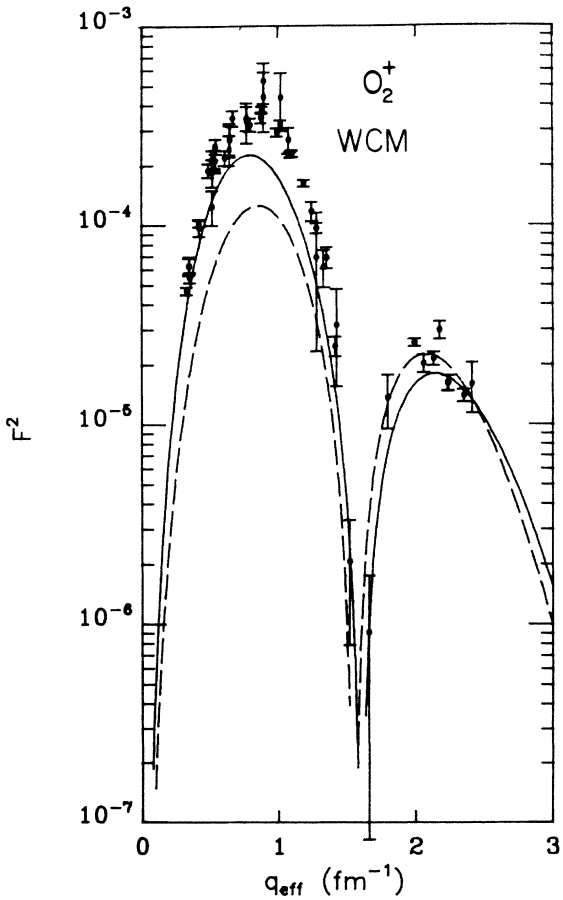


FIG. 22. The $0_2^+$ data are compared with WCM predictions using Woods-Saxon (solid) and harmonic oscillator (dashed) wave functions.

of the form factor to details of the radial density is most clearly illustrated using $r^2$ times the density, as plotted in Fig. 23. Orthogonality between initial and final states requires at least one node in a monopole transition density such that the integral of $r^2\rho$ vanishes. Perturbations of the radial density must conserve this integral. At a momentum transfer whose frequency matches the radial node, this small difference between the radial densities is amplified, thereby becoming a large difference in form factor. In the absence of a serious calculation of the single-particle wave functions, we cannot interpret this comparison as evidence favoring either choice. Rather, this level of sensitivity sets the scale of meaningful differences for models which do not explicitly calculate radial wave functions.

The WCM predictions for the quadrupole form factors are shown in Fig. 16; the densities are shown in Fig. 17. The magnitude of the density and form factor for the $2_1^+$ state is substantially underpredicted. The model prediction for the $2_3^+$ state is in gross disagreement with the data.

The WCM description of the shape of the $2_2^+$ density is good, but the strength is somewhat too large. For this state, the dominant transitions are between hole states within the $p$ shell.[75] These transitions are incapable of producing a form factor minimum, and therefore the predicted form factor is distinctly different from those states containing substantial $2s1d$ shell amplitudes. This picture is consistent with the core-excitation model which describes the state by a quadrupole excitation of the $^{12}C$ core coupled to a relative $s$ state between the core and an alpha cluster. A $p$-shell quadrupole core excitation, such as the first $2^+$ state in $^{12}C$, produces a qualitatively similar form factor.[54,55]

The fact that surface quadrupole transition strengths are underpredicted while the interior quadrupole transition strength is overpredicted suggests that no constant multiplicative polarization charge will suffice to reproduce the data.

The WCM prediction for the $4_1^+$ form factor is shown in Fig. 18. The density is shown in Fig. 19. It is clear that the magnitude of the WCM density is in reasonable agreement with the data, but that the radial scale is incorrect. Although this could be improved by adjusting the oscillator parameter, it is clear that a unique value will not improve the fit to all form factors.

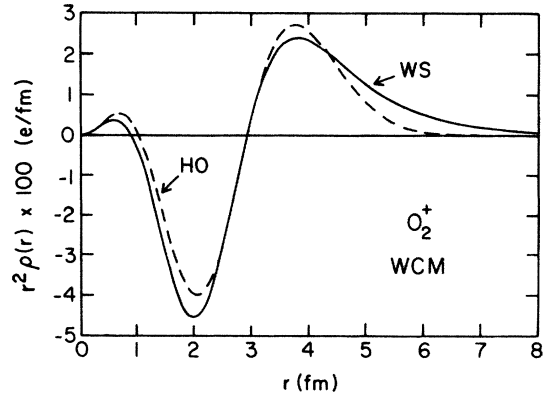


FIG. 23. Comparison between $0_2^+$ transition densities predicted by the WCM using the Woods-Saxon (solid) and harmonic oscillator (dashed) wave functions.

At the peak of the $4_2^+$ form factor, the experimental cross section is about 50 times greater than that predicted by the weak-coupling model. This represents a serious failure of the model. The WCM predicts similar 2p2h and 4p4h amplitudes for this state, with opposite signs, but the transfer-reaction data indicate that this state is predominantly 2p2h in character. Thus, the largest discrepancies observed between this model and the data occur in the 2p2h states near 11 MeV ($4_2^+$,$2_3^+$,$0_3^+$).

### C. $2\hbar\omega$ shell model

Amos *et al.*[22] recently reported a shell-model calculation for the dominantly 2p2h states near 11 MeV that employed a full $2\hbar\omega$ basis, including all orbitals up to $1f_{5/2}$. The Millener-Kurath interaction[76] was used. The spurious center-of-mass motion was eliminated from all 2p2h states. The energy spectrum was normalized to the $2_3^+$ state by subtracting 16.33 MeV. The adjusted energy of the $4_2^+$ state is then in good agreement with experiment, but the calculated energy of the state presumed to correspond with the observed $0_3^+$ state is about 4 MeV too low.[22] The dominantly 4p4h states below 11 MeV are beyond the scope of the model.

The $2_3^+$ and $4_2^+$ transition charge densities and form factors predicted by this model are shown as short-dashed lines in Figs. 16–19. These calculations used an oscillator parameter $b=1.77$ fm and no polarization charge. The longitudinal form factors are surprisingly accurate. The predicted transverse form factors are quite small, consistent with this experiment. It is unusual for a shell-model calculation to predict the strength of longitudinal form factors without invoking a renormalization parameter to "correct" for the truncation of the model space. However, this model predicts that $2\hbar\omega$ transitions between the $1p$ and the $2p1f$ shells dominate the electroexcitation of the $2_3^+$ and $4_2^+$ states. Similar results have been obtained for other nuclei in the $sd$ shell.[77] This basis is apparently sufficiently large to encompass most of the important contributions and need not be supplemented by an empirical renormalization factor. Moreover, unlike small-basis calculations, there are enough amplitudes to suppress the spin and current densities. The dominance of $2\hbar\omega$ transitions explains the fact that the weak-coupling model, even after including a polarization charge, predicts far too little strength to the $2_3^+$ and $4_2^+$ states—the basis employed by the WCM is too limited.

As shown in Figs. 14 and 15, the monopole transition density predicted by this model is approximately twice the experimental density. This discrepancy is probably related to the discrepancy in the energy calculated for this state, and may indicate that the neglected 4p4h components play an important role. Despite its smaller basis, the weak-coupling model does include 4p4h components and provides a better description of this state (if an effective charge is included).

Therefore, it appears that future shell-model calculations of the positive-parity states of $^{16}O$ must include 4p4h excitations but may be limited to the present $2\hbar\omega$ basis without serious loss.

### D. Tetrahedral $\alpha$-cluster model

Many $\alpha$-cluster descriptions of $^{16}O$ have been attempted, but very few electromagnetic form factors have been calculated from this point of view. A notable exception is the tetrahedral $\alpha$-cluster model of Robson,[17] which is of current interest because of its prediction of a new $3^-$ state unresolved from the $2_2^+$ state.

The model describes the $^{16}O$ ground state as a tetrahedral equilibrium configuration of four $\alpha$ clusters, each of which exhibits a similar tetrahedral internal structure. The ground-state rotational band of a rigid tetrahedron has the spin-parity sequence $0^+,3^-,4^+,6^+,7^-,8^+,\ldots$. Additional rotational bands can be based upon normal modes of vibration. The lowest such band exhibits the sequence $1^-,2^+,3^+,4^+,3^-,\ldots$. After fitting the coefficients of perturbative terms in the Hamiltonian to selected energy levels, a reasonable description of the $^{16}O$ spectrum is obtained, with some reordering of the pure rotation-vibration sequence.[17]

Robson has calculated charge form factors for several members of the ground-state rotational band, assuming that the wave function factorizes as a product of an internal wave function and a rotational wave function. In this model, the form factor reduces to

$$F_J(q)=C_J j_J(qR)F_v(q)\ , \tag{23}$$

where the coefficients $C_J$ are specified by the model and $F_v$ is the zero-point vibrational form factor. The radial parameter $R$ was determined by the $\alpha$-particle radius and a close-packing assumption. The vibrational form factor $F_v$ was fitted to the $^{16}O$ elastic scattering data, thus completing the model.[17]

The predicted $3_1^-$ and $4_1^+$ form factors are compared with the data in Fig. 24. The tetrahedral model reproduces both transition strengths and describes the form factors adequately for momentum transfers below about 1 $fm^{-1}$. However, for larger momentum transfer, the predicted form factors become much larger than the data. This discrepancy is much more severe for the $4_1^+$ state than for the $3_1^-$ state. If we assume that the dominant cluster configuration retains the same geometry in these states, then these comparisons suggest that the tetrahedral configuration is not rigid but stretches as the rotational frequency increases. The simplistic factorization approximation used by Robson[17] to compute the form factors precludes a definitive evaluation of the stability of the tetrahedral configuration.

A unique prediction of the tetrahedral $\alpha$-cluster model is the existence of a new narrow $3^-$ state at $9.90\pm0.07$ MeV, nearly degenerate with the known $2_2^+$ state at 9.847 MeV. Recently, several new experiments have sought this predicted $3^-$ state. Frawley *et al.*[79] remeasured the resonance elastic scattering of $\alpha$ particles from $^{12}C$ and concluded that either the new state has an $\alpha$ width $\Gamma<100$ eV or that it lies within a few keV above the $2^+$ state with

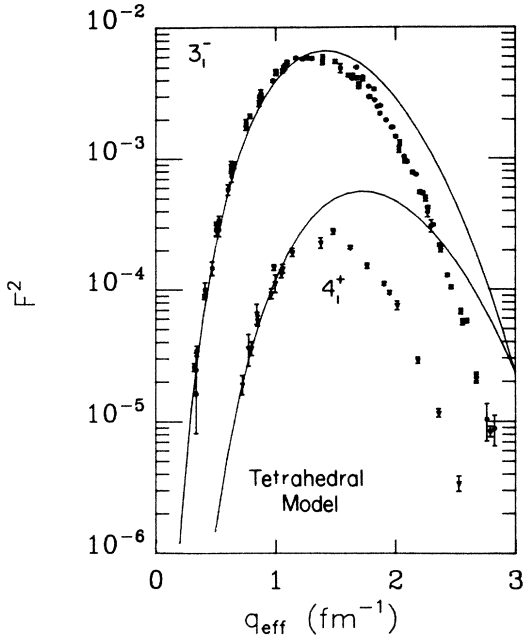


FIG. 24. Tetrahedral $\alpha$-cluster model predictions compared with $3_1^-$ and $4_1^+$ data. The corresponding figure in Ref. 17 contains a computational error (Ref. 78).

a width $\Gamma<150$ eV. Later, Frawley *et al.*[80] performed an angular correlation experiment for the $^{16}O(\alpha,\alpha')^{16}O^*(\alpha_0)^{12}C$ reaction. This experiment provided compelling evidence that a new $3^-$ state does not exist in the vicinity of 9.85 MeV. Finally, Kovash *et al.*[81] compared the resonance energies obtained in the $^{12}C(\alpha,\alpha)$ and $^{12}C(\alpha,\gamma)$ reactions and concluded that the separation of the putative doublet could be no greater than 1 keV. Furthermore, the $E1$ radiative decay width of a new $3^-$ state to the $2_1^+$ state must be less than $5\times10^{-4}$ eV.[80] The predicted $3^-$ state is in the same rotational band as the $2_1^+$ state and thus we would expect its $E1$ decay to the $2_1^+$ state to be enhanced, especially over a direct $E3$ decay to the ground state. Therefore, the preponderance of experimental data repudiates the predicted state.

Although the ground state may be well described by a tetrahedral $\alpha$-cluster configuration, the stretching exhibited by its rotational band demonstrates that this configuration is not rigid. This interpretation is, of course, consistent with the existence of an $\alpha$-decay threshold at only 7.16 MeV. The system may not be capable of sustaining the large-amplitude vibrations predicted for the lowest vibration-rotation band. It is also possible that a transition to a configuration of different symmetry, such as the planar "kite" configuration, occurs in the excited states.

## VII. CONCLUSIONS

We have measured the electromagnetic form factors for all narrow normal-parity states of $^{16}O$ below 12.05 MeV of excitation up to a momentum transfer of 2.6 $fm^{-1}$. These data have provided precise measurements of the ra-

dial transition charge densities for two $0^+$ states, three $2^+$ states, two $4^+$ states, one $1^-$ state, and one $3^-$ state. The precision of these charge densities permits detailed evaluation of nuclear structure models.

The low-lying spectrum of $^{16}$O has long been a challenge to nuclear structure theory. A large variety of models have been proposed to explain spectroscopic data, but little attention has been given to the radial properties of excited states. The present measurements provide precise transition densities for many states and should serve as an incentive for more ambitious structure investigations.

A basic attribute of many models of $^{16}$O is the presence of collective bands built upon deformed intrinsic states. The character of such intrinsic states can be extracted only in the context of a specific model. For example, although the existence of deformation in $^{16}$O appears to be well established, the possible triaxial character of this deformation remains an open question.

The coexistence model of Brown and Green[6,7] provided early insights into the structure of $^{16}$O. However, the sparse data then available were insufficient to stimulate maximum development of the model. We now know that the correspondences made between model and physical states were occasionally erroneous. Many shortcuts were taken in the calculations. The unperturbed energies were treated as fitting parameters. There remains considerable room for further development of this model, including variational calculation of the deformation parameters and self-consistent calculation of energies and radial wave functions. A more detailed calculation of the radial densities is required before the assumption of axial symmetry can be evaluated. Moreover, electromagnetic form factors for the $K=2$ states have not as yet been calculated even in the present model. Presumably the $2_2^+$ form factor, for example, is amenable to such a description.

The ability of the simple core-excitation model to account for the energy level sequence is attractive.[11] Unfortunately, radial transition densities have been calculated for only a few cluster models. The simplifying assumptions of the tetrahedral $\alpha$-cluster model[17] apparently are too restrictive to achieve a good description of the actual structure of $^{16}$O. The less restrictive models of Suzuki *et al.*[12–14] and of Bauhoff *et al.*[18] have achieved general consistency with the available spectroscopic data, but have not yet been used to predict transition densities. We hope that the present data will challenge these models.

The results of shell-model calculations have generally corroborated the relative intensities of 2p2h and 4p4h components in the states described by the Brown-Green model. However, practical limitations have severely hampered the ability of spherical shell-model calculations to predict the electromagnetic properties of collective excitations. Bases confined to the $1p$ and $2s1d$ shells must be supplemented by an additional isoscalar polarization charge of about $1e$. However, no constant effective charge is adequate. Due to the large intrinsic deformation it postulates, the Brown-Green model does not require an empirical enhancement. Similarly, Kamimura's $\alpha$-cluster calculation,[82] using resonating-group methods, for the transition densities of $^{12}$C provides an adequate description of electron scattering data, also without renormalization. Similar results may be expected for modern cluster-model calculations of $^{16}$O.

The successes of the recent $2\hbar\omega$ shell-model calculation reported by Amos *et al.*[22,77] suggest that the spherical shell model may soon be capable of predicting electromagnetic transition densities. It appears that this $2\hbar\omega$ basis contains most of the important contributions and thus need not be substantially renormalized. However, the calculations which were reported neglected important 4p4h contributions. We hope that a broader description of the structure of $^{16}$O will emerge as it becomes possible to include 4p4h configurations in a $2\hbar\omega$ shell-model calculation. However, quantitative comparisons will also require a realistic treatment of the radial wave functions.

The success of a nuclear structure theory must be judged on its description of experimental densities, as well as its ability to reproduce energy levels and transition rates. Although the individual models exhibit some success in fitting specific features of the data, none of them can fairly be said to successfully describe the richness and variety of the structure we have observed in $^{16}$O.

## ACKNOWLEDGMENTS

We would like to express our appreciation to Lyman Stinson and the entire staff of the Bates Linac for providing the technical support essential to the success of this experiment. We also thank Dr. Steven Williamson for providing us a version of the computer code HADES. We thank Dr. Jochen Heisenberg and Dr. Michael Mueller for assistance in using their programs. This work was performed under the auspices of the U. S. Department of Energy and of the National Science Foundation.

---

[a]Present address: Harris Semiconductor, Mail Stop 51-180, Melbourne, FL 32901.

[b]Present address: Department of Physics and Astronomy, University of Maryland, College Park, MD 20742.

[c]Present address: Department of Physics, College of William and Mary, Williamsburg, VA 23189.

[d]Present address: Department of Physics, University of New Hampshire, Durham, NH 03824.

[e]Present address: Los Alamos National Laboratory, Los Alamos, NM 87544.

[f]Present address: Department of Physics, University of Kentucky, Lexington, KY 40506.

[g]Present address: Tektronics Inc., Beaverton, OR 97077.

[h]Present address: Department of Physics, University of Virginia, Charlottesville, VA 22901.

[i]Present address: Department of Physics, George Washington

University, Washington, D.C. 20052.
[1]E. B. Carter, G. E. Mitchel, and R. H. Davis, Phys. Rev. **133**, B1421 (1964); **133**, B1434 (1964).
[2]J. Lowe, A. R. Poletti, and D. H. Wilkinson, Phys. Rev. **148**, 1045 (1966).
[3]D. H. Wilkinson, D. E. Alburger, and J. Lowe, Phys. Rev. **173**, 995 (1968); J. Lowe, D. E. Alburger, and D. H. Wilkinson, *ibid.* **163**, 1060 (1967).
[4]F. Ajzenberg-Selove, Nucl. Phys. **A375**, 1 (1982).
[5]G. E. Brown and A. M. Green, Nucl. Phys. **75**, 401 (1966).
[6]G. E. Brown and A. M. Green, Phys. Lett. **15**, 168 (1965).
[7]P. Goldhammer and F. W. Prosser, Phys. Rev. **163**, B950 (1967).
[8]J. C. Bergstrom, W. Bertozzi, S. Kowalski, X. K. Maruyama, J. W. Lightbody, S. P. Fivozinsky, and S. Penner, Phys. Rev. Lett. **24**, 152 (1970).
[9]A. S. Davydov and G. F. Filippov, Nucl. Phys. **8**, 237 (1958); A. S. Davydov and V. S. Rostovsky, *ibid.* **12**, 58 (1959).
[10]J. C. Bergstrom, I. P. Auer, F. J. Kline, and H. S. Caplan, Nucl. Phys. **A213**, 609 (1973).
[11]L. L. Ames, Phys. Rev. C **25**, 729 (1982).
[12]Y. Suzuki and B. Imanishi, Phys. Rev. C **23**, 2414 (1981).
[13]Y. Suzuki, T. Ando, and B. Imanishi, Nucl. Phys. **A295**, 365 (1978).
[14]Y. Suzuki, Prog. Theor. Phys. **55**, 1751 (1976); **56**, 111 (1976).
[15]B. Buck and J. A. Rubio, J. Phys. G **10**, L209 (1984).
[16]B. Buck, C. B. Dover, and J. P. Vary, Phys. Rev. C **11**, 1803 (1975).
[17]D. Robson, Phys. Rev. Lett. **42**, 876 (1979); Phys. Rev. C **25**, 1108 (1982).
[18]W. Bauhoff, H. Schultheis, and R. Schultheis, Phys. Rev. C **29**, 1046 (1984).
[19]A. P. Zuker, B. Buck, and J. B. McGrory, Phys. Rev. Lett. **21**, 39 (1968).
[20]B. S. Reehal and B. H. Wildenthal, Part. Nucl. **6**, 137 (1973).
[21]P. J. Ellis and T. Engeland, Nucl. Phys. **A144**, 161 (1970); T. Engeland and P. J. Ellis, *ibid.* **A181**, 368 (1972).
[22]K. Amos, W. Bauhoff, I. Morrison, S. F. Collins, R. S. Henderson, B. M. Spicer, G. G. Shute, V. C. Officer, D. W. Devins, D. L. Friesel, and W. P. Jones, Nucl. Phys. **A413**, 255 (1984).
[23]B. E. Norum, M. V. Hynes, H. Miska, W. Bertozzi, J. Kelly, S. Kowalski, F. N. Rad, C. P. Sargent, T. Sasanuma, W. Turchinetz, and B. L. Berman, Phys. Rev. C **25**, 1778 (1982).
[24]H. Miska, B. Norum, M. V. Hynes, W. Bertozzi, S. Kowalski, F. N. Rad, C. P. Sargent, T. Sasanuma, and B. L. Berman, Phys. Lett. **83B**, 165 (1979).
[25]C. E. Hyde-Wright *et al.* (unpublished).
[26]T. DeForest and J. D. Walecka, Adv. Phys. **15**, 1 (1966).
[27]S. T. Tuan, L. E. Wright, and D. S. Onley, Nucl. Instrum. Methods **60**, 70 (1968).
[28]J. M. Eisenberg and W. Greiner, *Excitation Mechanisms of the Nucleus* (North-Holland, Amsterdam, 1970).
[29]G. R. Hammerstein, R. H. Howell, and F. Petrovich, Nucl. Phys. **A213**, 45 (1973).
[30]W. Bertozzi *et al.*, IEEE Trans. Nucl. Sci. **NS-14**, 191 (1967).
[31]W. Bertozzi, M. V. Hynes, C. P. Sargent, C. Creswell, P. C. Dunn, A. Hirsch, M. Leitch, B. Norum, F. N. Rad, and T. Sasanuma, Nucl. Instrum. Methods **141**, 457 (1977).
[32]W. Bertozzi, M. V. Hynes, C. P. Sargent, W. Turchinetz, and C. Williamson, Nucl. Instrum. Methods **162**, 211 (1979).
[33]P. C. Dunn, Nucl. Instrum. Methods **165**, 163 (1979).
[34]T. N. Buti, Ph.D. thesis, Massachusetts Institute of Technology, 1984.
[35]F. W. Hersman, Ph.D. thesis, Massachusetts Institute of Technology, 1982.
[36]J. Kelly (unpublished).
[37]C. E. Hyde-Wright, Ph.D. thesis, Massachusetts Institute of Technology, 1984.
[38]W. Gentleman and G. Sande, in *Proceedings of the 1966 Fall Joint Computer Conference, San Francisco,* edited by R. G. Glaser (Spartan, Washington, D.C., 1967), p. 563.
[39]L. C. Maximon, Rev. Mod. Phys. **41**, 193 (1969).
[40]M. W. Deady, Ph.D. thesis, Massachusetts Institute of Technology, 1981.
[41]L. W. Mo and Y. S. Tsai, Rev. Mod. Phys. **41**, 205 (1969).
[42]J. Bergstrom, in Medium Energy Nuclear Physics with Electron Linear Accelerators, edited by W. Bertozzi and S. Kowalski, U.S. Department of Commerce Report TID-24667, 1967, p. 251.
[43]C. Creswell, LNS-MIT Internal Report 761, 1976.
[44]P. R. Bevington, *Data Reduction and Error Analysis for the Physical Sciences* (McGraw-Hill, New York, 1969), p. 248.
[45]J. Kelly, Ph.D. thesis, Massachusetts Institute of Technology, 1981.
[46]M. V. Hynes, J. Kelly, B. W. Peterson, and B. E. Norum, submitted to Nucl. Instrum. Methods.
[47]I. Sick and J. S. McCarthy, Nucl. Phys. **A150**, 631 (1970).
[48]W. Schutz, Z. Phys. A **273**, 69 (1975).
[49]J. F. Ziegler, Yale University Report 2726E-49, 1967.
[50]See AIP document no. PAPS PRVCA-33-755-18 for 18 pages containing a complete tabulation of the data described in this paper. Order by PAPS number and journal reference from American Institute of Physics, Physics Auxiliary Publication Service, 335 E. 45th Street, New York, NY 10017. The price is $1.50 for each microfiche (98 pages) or $5.00 for photocopies of up to 30 pages, and $0.15 for each additional page over 30 pages. Airmail additional. Make checks payable to the American Institute of Physics.
[51]J. Heisenberg and H. P. Blok, Annu. Rev. Nucl. Part. Sci. **33**, 569 (1983).
[52]J. Heisenberg (unpublished).
[53]H. G. Andersen, H. Peter, M. Mueller, and H. J. Ohlbach (unpublished).
[54]H. Crannell, Phys. Rev. **148**, 1107 (1966).
[55]M. Stroetzel, Z. Phys. **214**, 357 (1968); Phys. Lett. **26B**, 376 (1968).
[56]X. K. Maruyama, Ph.D. thesis, Massachusetts Institute of Technology, 1971.
[57]J. C. Bergstrom and I. P. Auer, Nucl. Phys. **A215**, 232 (1973).
[58]H. Miska, H. D. Graf, A. Richter, R. Schneider, D. Schull, E. Spamer, H. Thiessen, and O. Titze, Phys. Lett. **58B**, 155 (1975).
[59]H. Miska, H. D. Graf, A. Richter, D. Schull, E. Spamer, and O. Titze, Phys. Lett. **59B**, 441 (1975).
[60]G. R. Bishop, C. Betourne, and D. B. Isabelle, Nucl. Phys. **53**, 366 (1964).
[61]Y. Torizuka, M. Oyamada, K. Nakahara, K. Sugiyama, Y. Kojima, T. Terasawa, K. Itoh, A. Yamaguchi, and M. Kimura, Phys. Rev. Lett. **22**, 594 (1969).
[62]J. C. Kim, R. P. Singhal, and H. S. Caplan, Can. J. Phys. **48**, 83 (1970).
[63]J. Heisenberg, Adv. Nucl. Phys. **12**, 61 (1981).
[64]B. Dreher, J. Friedrich, K. Merle, H. Rothhaas, and G. Luhrs, Nucl. Phys. **A235**, 219 (1974).
[65]J. B. Flanz, R. S. Hicks, R. A. Lindgren, G. A. Peterson, A. Hotta, B. Parker, and R. C. York, Phys. Rev. Lett. **41**, 1642

(1978).
[66]E. Rost and G. E. Brown, Bull. Am. Phys. Soc. **10**, 487 (1965).
[67]W. H. Bassichis and G. Ripka, Phys. Lett. **15**, 320 (1965).
[68]T. Erikson, Nucl. Phys. **A170**, 513 (1971).
[69]T. Erikson, Nucl. Phys. **A211**, 105 (1973).
[70]T. P. Marvin and P. P. Singh, Nucl. Phys. **A180**, 282 (1972).
[71]M. D'Agostino Bruno, I. Massa, A. Uguzzoni, G. Vannini, E. Verondini, and A. Vitale, Nuovo Cimento **27**, 1 (1975).
[72]M. S. Zisman, E. A. McClatchie, and B. G. Harvey, Phys. Rev. C **2**, 1271 (1970).
[73]J. Lowe and A. R. Barnett, Nucl. Phys. **A187**, 323 (1972).
[74]F. D. Becchetti, D. Overway, J. Jänecke, and W. W. Jacobs, Nucl. Phys. **A344**, 336 (1980).
[75]V. Horsfjord, Nucl. Phys. **A209**, 493 (1973).
[76]D. J. Millener and D. Kurath, Nucl. Phys. **A255**, 315 (1975).
[77]K. Amos and W. Bauhoff, Nucl. Phys. **A424**, 60 (1984).
[78]D. Robson, private communication.
[79]A. D. Frawley, J. D. Fox, K. W. Kemper, and L. C. Dennis, Phys. Rev. C **25**, 2935 (1982).
[80]A. D. Frawley, J. D. Fox, L. C. Dennis, K. W. Kemper, and N. R. Fletcher, Phys. Rev. C **27**, 2482 (1983).
[81]M. A. Kovash, R. W. Lourie, W. Pugh, C. E. Hyde-Wright, D. G. Marchlenski, H. R. Suiter, J. C. Brown, and R. G. Seyler, Phys. Rev. C **31**, 1065 (1985).
[82]M. Kamimura, Nucl. Phys. **A351**, 456 (1981).